Applied Thermal Engineering 283 (2026) 129008

Contents lists available at ScienceDirect

Applied Thermal Engineering

journal homepage: www.elsevier.com/locate/apthermeng

Research Paper

Flow boiling in micro-pin fin heat exchangers and comparison with correlations

Ali H. Al-Zaidi [a], Tassos G. Karayiannis [b,*]

[a] University of Misan, Al-Amarah 62001, Iraq
[b] Department of Mechanical and Aerospace Engineering, Brunel University of London, Uxbridge UB8 3PH, UK

ARTICLE INFO

Keywords:
Flow patterns
Heat transfer
Pressure drop
Hysteresis
Micro-pin fins
Electronics cooling
Correlations

ABSTRACT

The thermo-fluid performance of micro-pin fin heat exchangers has recently received extensive attention from the research community engaged in developing thermal management systems for high heat flux devices. Two-phase flow in these geometries could provide better thermal performance compared to other designs. However, more studies are still required to understand the effect of the control parameters on the fundamental flow boiling characteristics. Therefore, the present study aimed to examine experimentally the performance of micro-pin fin heat exchangers at different operating conditions. Staggered diamond micro-pin fins having a pin height of 1 mm and pin width of 0.6 mm were manufactured on a total base area of 20 mm × 25 mm. HFE-7100 was tested at a system pressure (inlet pressure) of 1, 1.5 and 2 bar, mass flux from 100 to 250 kg/m^2 s and 5 K inlet sub-cooling, while the wall heat flux was varied up to 324 kW/m^2. The heat flux was increased gradually until the maximum thermal limit was achieved. Flow pattern features and bubble nucleation around the pins were visualised using a high-speed, high-resolution camera. A base heat flux up to 0.63 MW/m^2 was recorded without reaching the dryout region or the critical heat flux. Low substrate surface temperature, i.e. less than 85 °C, and stable flow without flow reversal and hysteresis were achieved in this geometry, making flow boiling in micro-pin fin heat sinks suitable for cooling electronics. Nucleate boiling was found to be present for the entire range studied. The effect of heat flux and pressure on the heat transfer rates was significant, while the mass flux effect was marginal for the range studied. Ten existing heat transfer and pressure drop correlations were evaluated, and a good prediction was found by some of them. The prediction of the pressure drop by existing correlations improved when the pin dimensions and the space between them was introduced in the two-phase friction multiplier.

1. Introduction

The continuous demand for efficient thermal management systems for the electronics sector encouraged researchers to propose and develop different cooling techniques, starting with single- phase air heat sinks and progressing to liquid systems. Further reductions in the chip size and increasing performance requirements have led to a new bottle neck, with the researchers and industrialist turning their attention to pumped two-phase flow systems, which can provide higher thermal performance, while keeping the substrate to be cooled within operational design temperatures. In addition, advanced manufacturing technologies facilitated the design and production of more complicated geometries in the micro-scales. These different geometries were tested with working fluids and operating conditions in the search for heat sinks that can dissipate the increasing thermal load. For example, rectangular multi-microchannels [1,2], diverging microchannels [3], micro-gaps [4] and micro-pin fins heat sinks were designed and examined. Single and two-phase flows in micro-pin fins have been extensively studied. Table 1 and Fig. 1 include different pin geometries proposed in the literature such as circular, square, diamond, honeycombed, pentagonal, triangle, inverted triangle, oblique, hydrofoil and streamline shapes. More complicated geometries were also proposed such as latticed, petaloid, open-ring and piranha. Different pin arrangements, in-line or staggered, were also examined, see Fig. 2. These different geometries and arrangements could lead to different fluid mixing processes and then different heat transfer rates and pressure drop.

Bhandari et al. [27] and Mertens et al. [28] presented recent reviews on numerical and experimental studies. However, clarification on the work presented is needed before comparative conclusions can be drawn

* Corresponding author at: Department of Mechanical and Aerospace Engineering, Brunel University of London, Uxbridge, Middlesex UB8 3PH, UK.
E-mail address: tassos.karayiannis@brunel.ac.uk (T.G. Karayiannis).

https://doi.org/10.1016/j.applthermaleng.2025.129008
Received 3 August 2025; Received in revised form 3 October 2025; Accepted 4 November 2025
Available online 5 November 2025

Nomenclature

A	Area, [m^2]
Bo	Boiling number, [-],$Bo = q''/Gi_{lg}$
C	Chisholm parameter, [-]
cp	Specific heat capacity, [J/kg K]
D	Diameter, [m]
D_h	Hydraulic diameter, [m]
dh	Clearance between pin tip and cover plate, [m]
f	Friction factor, [-]
F	Enhancement factor, [-]
Fr	Froude number, [-],$Fr = G^2/gD_h\rho_l^2$
g	Gravitational acceleration, [m/s^2]
G	Mass flux, [kg/m^2 s]
h	Heat transfer coefficient, [W/m^2 K]
$\overline{h}$	Average heat transfer coefficient, [W/m^2 K]
H	Height, [m]
i	Specific enthalpy, [J/kg]
i_{lg}	Latent heat of vaporization, [J/kg]
k	Thermal conductivity, [W/m K]
K_c	Contraction coefficient, [-]
K_e	Expansion coefficient, [-]
L	Length, [m]
La	Laplace number, [-],$La = \left(\sigma/g\Delta\rho D_{min}^2\right)^{0.5}$
m	Fin parameter, see Eq. (24), [-]
$\dot{m}$	Mass flow rate, [kg/s]
M	Molecular mass, [kg/kmol]
MAE	Mean absolute error, [%]
N	Number of data points, [-]
N_{ch}	Number of channels, [-]
N_{pin}	Number of pins, [-]
Nu	Average Nusselt number, [-],$Nu = \overline{h}D_h/k_l$
P	Pressure, [Pa]
P_R	Reduced pressure, [-]
Pr	Prandtl number, [-],$Pr = cp_l\mu_l/k_l$
q''	Heat flux, [W/m^2]
Ra	Average surface roughness, [μm]
Re	Reynolds number, [-], $Re = GD_h/\mu_l$
$R_{p,old}$	Old roughness parameter in Cooper's correlation, [μm]
S	Suppression factor, [-]
Sa	Average surface roughness of scanned area, [μm]
S_D	Diagonal pitch, [m]
S_L	Longitudinal pitch, [m]
S_T	Transverse pitch, [m]
T	Temperature, [K]
u	Velocity, [m/s]
U	Absolute uncertainty, [-]
v	Specific volume, [m^3/kg]
$\dot{v}$	Volume flow rate, [m^3/s]
W	Width, [m]
We	Weber number, [-],$We = G^2D_h/\sigma\rho_l$
x	Vapour quality, [-]
X	Lockhart–Martinelli parameter, [-]
Y	Vertical distance between first row of thermocouples and pins bottom, [m]
z	Distance measured from inlet to end of heated length, [m]

Greek symbols

α	Void fraction, [-]
β	Fin density, [-]
ΔP	Pressure drop, [Pa]
ΔT	Temperature difference, [K]
ε	Local loss factor, [-]
η	Fin efficiency, [-]
θ	Angle, [°]
λ	Adjustment factor, [-]
μ	Viscosity, [Pa s]
ξ	Two-phase multiplier, [-]
ρ	Density, [kg/m^3]
σ	Surface tension, [N/m]
$\varnothing_l$	Two-phase friction multiplier, [-]
ω	Aspect ratio of pin, [-]

Subscripts

acc	Accelerational
b	Base
ch	Channel
cu	Copper
d	Darcy
exp	Experimental
fr	Frictional
g	Vapour, gravitational
h	Homogeneous
ht	Heat transfer
i	Inlet
l	Liquid
lg	Liquid to vapour
max	Maximum
$meas$	Measured
min	Minimum
nb	Nucleate boiling
o	Outlet
p	Plenum
pin	Pins
$pred$	Predicted
sat	Saturation
sc	Sudden contraction
se	Sudden expansion
sp	Single-phase
sub	Sub-cooled
sup	Superheat
th	Thermocouple
tp	Two-phase
w	Wall
z	Axial location

from these studies. The main points that can be deduced from the results of Table 1 are as follows:

Very complex pin shapes were tested by a number of researchers that could require high manufacturing and maintenance costs. Some of these designs are difficult to fabricate using metal heat sinks. A wide range of operating conditions was examined such as mass flux and inlet sub-cooling. However, very high mass flux can increase the total pressure drop and subsequently the pumping power required. High inlet sub-cooling could result in a significant part of the heat sink being in single-phase, i.e. not uniform surface bottom temperature. As a consequence, the electronic component to be cooled will not be in uniform temperature. High temperature and temperature non-uniformity are equally detrimental to the performance and the longevity of electronics. In an addition, high inlet sub-cooling will also require a larger condenser as part of the thermal management system. DI-water was used to achieve very high heat fluxes, but its relatively high freezing point could restrict its use in closed-loop cooling systems, i.e. expansion due to freezing can lead to system damage. In addition, the high boiling point at

Table 1
Two-phase flow studies using micro-pin fins reported in the literature.

Authors	Fluid(s)	Pin geometry	Pin dimensions [mm]	Operating conditions	Maximum base heat flux [kW/m^2]	Maximum surface temperature [°C]
Wan et al. [5]	De-ionized water	Staggered square, circular, diamond and streamline pins	W_{pin} = 0.4–0.5 H_{pin} = 0.54–0.58	ΔT_{sub} = 10 K G = 500 kg/m^2 s	850	ΔT_{sup} = 35
Deng et al. [6]	De-ionized water	In-line and staggered open-ring pins	D_{pin} = 3 H_{pin} = 0.7	ΔT_{sub} = 10 K G = 200 & 300 kg/m^2 s	1000	ΔT_{sup} = 36
Hsu et al. [7]	De-ionized water	In-line triangle, inverted triangle and circular pins	D_{pin} = 0.15 H_{pin} = 0.201	$\dot{m}$ = 0.51 kg/min	2550	ΔT_{sup} = 40
Markal et al. [8]	De-ionized water	In-line square pins	W_{pin} = 0.5 H_{pin} = 0.2	G = 98 kg/m^2 s	272	ΔT_{sup} = 3.7
Moreira et al. [9]	De-ionized water	In-line and staggered square pins	W_{pin} = 0.3 H_{pin} = 0.35	ΔT_{sub} = 10 & 20 K G = 1000 & 1200 kg/m^2 s	265(wall heat flux)	ΔT_{sup} = 7.75
Li et al. [10]	De-ionized water & HFE-7100	In-line circular pins integrated with parallel microchannels	W_{ch} = 0.2 H_{ch} = 0.25	G = 80–600 kg/m^2 s (for water) G = 231–2772 kg/m^2 s (for HFE-7100)	9440 (for water)2870 (for HFE-7100)	188.8 (for water)57.4 (for HFE-7100)
Reeser et al. [11]	De-ionized water & HFE-7200	Staggered diamond & in-line square pins	W_{pin} = 0.153 H_{pin} = 0.305	G = 400–1300 kg/m^2 s (for water) G = 200–600 kg/m^2 s (for HFE-7200)	1180 (for water)360 (for HFE-7200)	–
McNeil et al. [12]	R113	In-line square pins	W_{pin} = 1 H_{pin} = 1	G = 50–250 kg/m^2 s	140	–
Kosar and Peles [13]	R123	Staggered hydrofoil pins	W_{pin} = 0.1 H_{pin} = 0.243	G = 976–2349 kg/m^2 s	3120	≈138
Wang et al. [14]	R134a	Staggered honeycombed & petaloid pins	W_{pin} = 0.9 H_{pin} = 1.5	ΔT_{sub} = 5 K $\dot{v}$ = 1 & 1.5 L/min	200	≈43
Li et al. [15]	R134a	Staggered diamond pins	W_{pin} = 1 H_{pin} = 0.5 θ_{pin} = 30–90°	G = 200–500 kg/m^2 s	37.5(wall heat flux)	–
Yubing et al. [16]	R134a	Staggered diamond pins	W_{pin} = 1 H_{pin} = 0.5	G = 200–500 kg/m^2 s	30(wall heat flux)	–
Xu et al. [17]	R134a, R1234yf & R1234ze(E)	Staggered petaloid-diamond pins	W_{pin} = 0.6 H_{pin} = 0.4	G = 100–200 kg/m^2 s	40	–
Falsetti et al. [18]	R236fa	In-line circular pins	D_{pin} = 0.05 H_{pin} = 0.1	G = 500–2500 kg/m^2 s	480	–
Hu et al. [19]	Novec649	Staggered pentagonal pins	W_{pin} = 3.2 H_{pin} = 2	ΔT_{sub} = 14–34 K u_i = 0.1–0.9 m/s	400	≈75
Law and Lee [20]	FC-72	In-line oblique pins	W_{pin} = 0.25 H_{pin} = 1.17	T_i = 29.5 °C G = 175–350 kg/m^2 s	1200	≈130
Liu et al. [21]	FC-72	In-line square pins	W_{pin} = 0.03 H_{pin} = 0.06	ΔT_{sub} = 35 K u_i = 0.25–1 m/s	800	ΔT_{sup}≈5
Yu et al. [22]	HFE-7000	Staggered piranha pins	W_{pin} = 0.15 H_{pin} = 0.2	G = 618–2569 kg/m^2 s	7350	≈93
Nunes et al. [23]	HFE-7100	In-line square pins	W_{pin} = 0.3 H_{pin} = 0.16 & 0.35	ΔT_{sub} = 10 & 20 K G = 1000 & 1200 kg/m^2 s	186	ΔT_{sup} = 4
Zhuang et al. [24]	HFE-7100	In-line circular pins	D_{pin} = 0.3 H_{pin} = 0.3	ΔT_{sub} = 20–34 K G = 189–374 kg/m^2 s	2175	77.5
Ji et al. [25]	HFE-7100	In-line square pins	W_{pin} = 0.03 H_{pin} = 0.06	ΔT_{sub} = 40 K G = 760–3040 kg/m^2 s	2930	≈100

atmospheric pressure will require sub-atmospheric flow conditions in order the keep the temperature of the substrate, i.e. electronic component to be cooled, below 100 °C. In certain studies, non-eco-friendly (high GWP and ODP) working fluids were used, such as R113, R134a, R236fa and FC-72. In certain experiments included in the Table 1, the temperature of the surface to be cooled reached high levels (more than 100 °C for the tests with water, R123 and FC-72), which is not suitable for most electronics.

Although high base heat fluxes were achieved in some of these studies, the actual cooling capacity was found to be very small, i.e. the footprint area of the cooling device used in the experiments was very small. For example, a base heat flux of 2.87 MW/m^2 was reported by Li et al. [10] using HFE-7100. However, their footprint area was 2 mm × 10 mm, and the cooling capacity was found to be only 57.4 W. The maximum cooling capacity reported in this table was 293 W in the work of Ji et al. [25] with HFE-7100. The reported heat flux was 2.93 MW/m^2 for a heat sink with 10 mm × 10 mm total base area. Note however the high degree of sub-cooling in these experiments.

1.1. Heat transfer coefficient correlations

A number of correlations [11,13,16,24,29] were developed in the literature to calculate two-phase heat transfer coefficient in micro-scale pin geometries as shown in Appendix I. These correlations can be divided into three groups based on the dominant heat transfer mechanisms as follows:

1.1.1. Nucleate boiling mechanism

A group of researchers found that the nucleate boiling dominated during two-phase flow experiments. For example, Kosar and Peles [13] tested R123 in staggered hydrofoil pins having 0.1 mm width and 0.243 mm height. They carried out their experiments at a heat flux of 190–3120 kW/m^2 and mass flux of 976–2349 kg/m^2 s. They reported that, at low heat fluxes, the two-phase heat transfer coefficient strongly

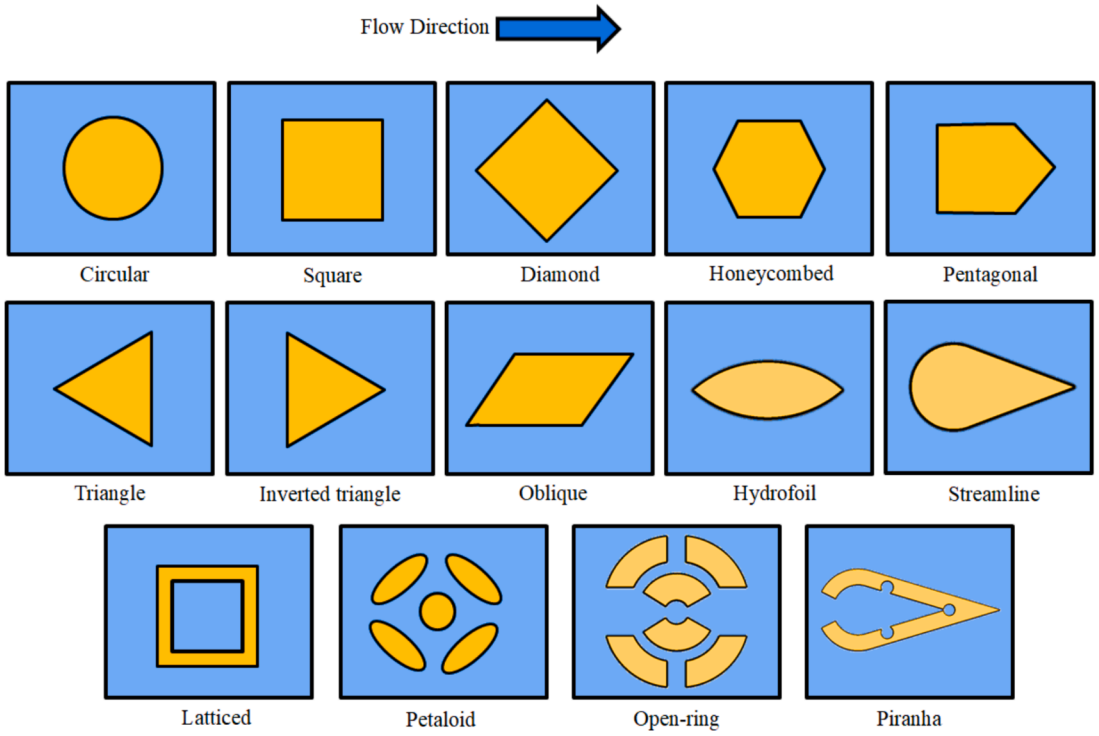

Fig. 1. Schematic diagram of different pin geometries reported in the literature, see Table 1. Latticed pins were reported by Wang et al. [26].

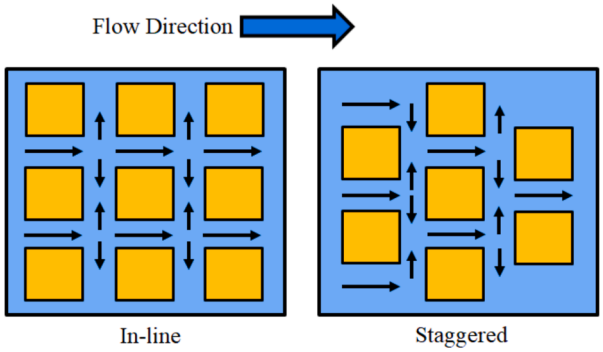

Fig. 2. Schematic diagram of different pin arrangements.

depended on the heat flux. Therefore, they correlated this data as a function of heat flux, and thus their correlation was recommended for the nucleate boiling mechanism. McNeil et al. [12] also found the dominance of this mechanism in flow boiling of R113 in in-line square pins having a pin height and width of 1 mm. They performed flow boiling experiments at a heat flux of 5–140 kW/m^2 and mass flux of 50–250 kg/m^2 s. Their results showed that the two-phase heat transfer coefficient depended on the heat flux and was independent of the vapour quality and mass flux.

1.1.2. Convective boiling mechanism

A number of researchers reported that the convective boiling could be the dominant heat transfer mechanism in their experiments. Kosar and Peles [13] in the same paper mentioned above, found that at high heat fluxes, the two-phase heat transfer coefficient was independent of heat flux, while the mass flux had a noticeable effect. They proposed another correlation for the convective mechanism by introducing the liquid Reynolds number. Reeser et al. [11] examined two fluids, namely DI-water and HFE-7200, in staggered diamond and in-line square pins with a pin width of 0.153 mm and height of 0.305 mm. In the HFE-7200 experiments, the heat flux was varied from 10–360 kW/m^2, while the mass flux was 200–600 kg/m^2 s. It was found that, at exit vapour quality up to 0.15, the two-phase heat transfer coefficient decreased with increasing vapour quality. They suggested that this reduction could be due to the change in flow patterns from bubbly to slug flow. However, at a vapour quality up to 0.4–0.5, the two-phase heat transfer coefficient was found to be flat or slightly increased with quality. They explained this based on the existence of annular flow and then thin liquid film evaporation. At higher exit vapour qualities, the two-phase heat transfer coefficient sharply decreased due to the dryout region during annular flow. Their results also showed that the two-phase heat transfer coefficient increased with mass flux during annular flow at exit vapour qualities of 0.15–0.5. They correlated their data as a function of the exit vapour quality, mass flux, two-phase multiplier (Lockhart–Martinelli parameter), and single-phase heat transfer coefficient.

1.1.3. Nucleate and convective boiling mechanisms

The presence of nucleate and convective heat transfer mechanisms were reported by several researchers in the literature. For instance, Yubing et al. [16] carried out flow boiling experiments of R134a in staggered diamond pins with 1 mm width and 0.5 mm height. These experiments were set at 15–30 kW/m^2 heat flux and 200–500 kg/m^2 s mass flux. It was found that, at low local vapour qualities, the local heat transfer coefficient increased with heat flux, and was independent of vapour quality. In contrast, at moderate and high local vapour qualities, the local heat transfer coefficient was found to increase with quality and was independent of heat flux. An increase in the mass flux led to an increase in the heat transfer coefficient. They adopted the Liu-Winterton correlation to include the contributions of nucleate and convective boiling components. They used the Cooper correlation [29] to represent the nucleate boiling mechanism. They also correlated the enhancement factor F as a function of the two-phase multiplier and fin density. The liquid Weber number was also included in the suppression factor S. The effect of pin dimensions and pin spacing were considered in their correlation. Zhuang et al. [24] examined flow boiling of HFE-7100 in in-line circular pins having 0.3 mm height and 0.3 mm diameter. They tested

this working fluid at a heat flux of 17–239 kW/m^2 and mass flux of 189–374 kg/m^2 s. They found that, at low heat fluxes, the local heat transfer coefficient increased with heat flux, and decreased with increasing mass flux. They mentioned that the nucleate boiling dominated at these low heat fluxes. However, at high heat fluxes, the local heat transfer coefficient increased with mass flux, while slightly decreased or flattened out with heat flux leading to report that the convective boiling mechanism was the dominant mechanism. When they reached the critical heat flux, a sharp reduction in the local heat transfer coefficient was found. They used their experimental data to modify the correlation by Reeser et al. [11].

It can be concluded that different heat transfer mechanisms and subsequently dependency of the heat transfer rates on different control parameters were reported in the literature. This can lead to different empirical constants, exponents and then proposed correlations. It can limit the predictive capabilities of the proposed correlations to specific working fluid(s), operating conditions and pin geometry/size.

1.2. Pressure drop correlations

The effect of different parameters on the two-phase pressure drop results is less complex than that on heat transfer results. It is generally agreed in the literature that the two-phase pressure drop increased with increasing heat flux or vapour quality and mass flux, see Reeser et al. [11], Zhuang et al. [24], Li et al. [15] and Xu et al. [17]. The experimental studies by Li et al. [15] and Xu et al. [17] showed that the two-phase pressure drop increased with decreasing inlet pressure. Zhuang et al. [24] found that, for a given heat flux, increasing inlet sub-cooling led to a reduction in the pressure drop across the pins array (total pressure drop including single and two-phase flow) due to the smaller single-phase pressure drop component which contributes to the total pressure drop.

The effect of pin dimensions and arrangements are the geometric parameters considered by the researcher community. Reeser et al. [11] in their experimental results showed that the two-phase pressure drop in the staggered arrangement was larger than that in the in-line arrangement. Li et al. [15] tested R134a in staggered diamond pins having a pin width of 1 mm, height of 0.5 mm, different pin length of 1–3.73 mm and angle of 30–90°. The flow boiling experiments were carried out at a heat flux of 10–37.5 kW/m^2 and mass flux of 200–500 kg/m^2 s. They found that the two-phase pressure drop increased with increasing fin density, fin angle and decreasing the diagonal space between pins.

Different fluid properties could also result in different two-phase pressure drop results. Xu et al. [17] examined three different working fluids namely R1234yf, R1234ze(E) and R134a in staggered petaloid-diamond pins. It was found that R134a had the highest pressure drop compared to other fluids. In contrast, R1234ze(E) provided the lowest two-phase pressure drop results.

Generally, two-phase pressure drop in heat exchangers includes three components as shown in Eq. (1).

$$\Delta P_{tp} = \Delta P_g + \Delta P_{fr} + \Delta P_{acc} \tag{1}$$

For horizontal heat exchangers, the gravitational pressure drop component ΔP_g is zero. The frictional pressure drop component ΔP_{fr} is found from the Lockhart–Martinelli separated flow method by calculating the frictional pressure gradient of two-phase flow in pipes, see Thome and Cioncolini [30].

$$\left(\frac{dP}{dz}\right)_{fr} = \frac{2f_l G^2 (1-x)^2}{\rho_l D_h} \varnothing_l^2 \tag{2}$$

The two-phase friction multiplier $\varnothing_l^2$ was correlated by Chisholm [31] as follows:

$$\varnothing_l^2 = 1 + \frac{C}{X} + \frac{1}{X^2} \tag{3}$$

where C is the Chisholm parameter. This method was also adopted in pin heat exchangers, and thus the Chisholm parameter or the two-phase friction multiplier was correlated by researchers based on their experimental data as presented in Appendix I. The Lockhart–Martinelli parameter is calculated from Eq. (4).

$$X = \sqrt{f_{l(d)} \frac{G_{max}^2 (1-x)^2}{2\rho_l} / f_{g(d)} \frac{G_{max}^2 x^2}{2\rho_g}} \tag{4}$$

It is worth mentioning that, the liquid and vapour single-phase Darcy friction factor $f_{l(d)}$ and $f_{g(d)}$ are adopted in these correlations. These friction factors are calculated at the liquid and vapour Reynolds number using the maximum mass flux and the hydraulic diameter of the pin cross-sectional area, see Appendix I for more details. The accelerational pressure drop component is calculated as follows:

$$\Delta P_{acc} = \frac{G_{min}^2}{\rho_l} \left[\frac{x^2}{\alpha} \left(\frac{\rho_l}{\rho_g} \right) + \frac{(1-x)^2}{1-x} - 1 \right] \tag{5}$$

The minimum mass flux is found from Eq. (6).

$$G_{min} = \frac{\dot{m}}{A_{max}} \tag{6}$$

$$A_{max} = W_b H_{pin} \tag{7}$$

in Eq. (5), the void fraction proposed by Zivi [32] is widely used in the literature.

$$\alpha = \left[1 + \frac{1-x}{x} \left(\frac{\rho_g}{\rho_l} \right)^{0.67} \right]^{-1} \tag{8}$$

The Chisholm parameter was proposed as a different empirical constant in the correlations by Reeser et al. [11], Zhuang et al. [24] and Xu et al. [17]. However, in other correlations the pin dimensions were introduced affecting the Chisholm constant. For example, the fin density and the aspect ratio of pins were included in the Chisholm parameter by Li et al. [15]. Xu et al. [17] introduced the Laplace constant, as a function of pin dimensions, in the two-phase friction multiplier. The different approach and values relating to the Chisholm parameter is probably due to different experimental conditions, including different fluids, operating conditions and pin dimensions, and the derived results that were used to obtain these parameters.

The abovementioned review indicates that further investigation is still required on flow boiling in micro-scale pin heat exchangers. Different working fluids, pin geometries/dimensions and operating conditions could result in different heat transfer mechanisms and control parameters. Following that, the objectives of the present study can be summarised as follows:

1. Examine the effect of heat flux, mass flux and inlet pressure on the flow boiling patterns, boiling heat transfer and pressure drop in micro-pin fin heat exchangers.
2. Analyse the complex features of flow patterns produced by the pins under different operating conditions and locations using a high-speed, high-resolution camera.
3. Assess existing correlations for calculating two-phase heat transfer coefficient and pressure drop. This could contribute to design guidance for similar geometries used in electronics cooling.
4. Identify the dominant heat transfer mechanism and the control parameters in the present flow boiling investigation. This could help in developing new design correlations or enhancing overall thermal performance.

The novelty of the present study compared with past research is outlined below:

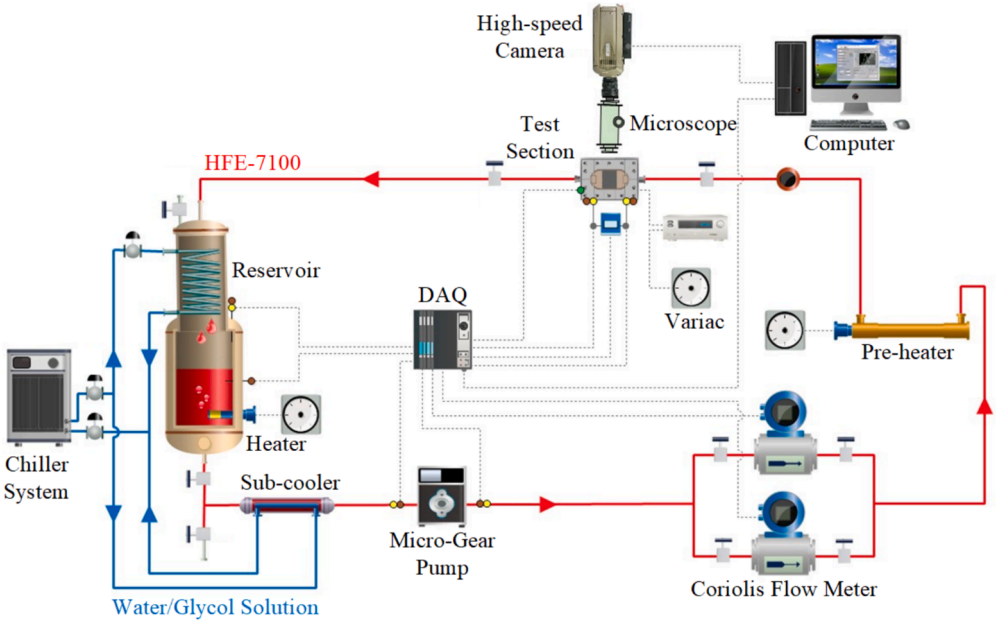

Fig. 3. Schematic diagram of the experimental facility, [33].

1. Semi-circular manifolds and the heated area of the pins were designed as a single integrated component. This unique heat sink design offers two advantages: (1) uniform flow distribution within the manifolds, and (2) ease of attachment to any chipset, making it suitable for commercial applications. The base area of this heat sink was designed to be 20 mm × 25 mm, which covers the die size of most chipsets. Staggered diamond pins were adopted in our study by taking into account the design recommendations by Bhandari et al. [27]. They showed that pins with sharp edges and staggered arrangements can enhance overall thermal performance by improving fluid mixing process.
2. One of the aims of the work was to reach and record maximum base heat flux at low operating conditions that can easily be applied in actual designs, i.e. very low inlet sub-cooling, mass flux and operating pressures.
3. The current work seeks to demonstrate stable thermal performance operating below or near critical heat flux, with a maximum surface temperature (less that 100 °C) that would allow use of the technique in cooling of electronics and assess if flow reversal or hysteresis occur.
4. The flow patterns in these pin arrays were examined to understand and confirm the influence of pins on flow features and then heat transfer results, which could contribute to discrepancies in experimental results reported in the literature.

The present flow boiling experiments were carried out using HFE-7100 at different inlet pressures of 1, 1.5 and 2 bar, mass fluxes from 100 to 250 kg/m^2 s and very low inlet sub-cooling of 5 K. The input heating power was gradually increased until the exit vapor quality was close to one, indicating the maximum thermal limits.

2. Experimental system and procedure

2.1. Experimental facility

Fig. 3 depicts the schematic diagram of the experimental rig used in this study, while further details are included in [33]. Most parts of this experimental facility were made of stainless steel to prevent any reaction with the working fluid and the rig components. All the measuring sensors and instruments such as thermocouples, pressure transducers and mass flow meters were carefully calibrated before connecting to the rig. A data logger (National Instruments) with a processing speed of 1 kHz was used to record all the signals from the rig sensors and instruments. The LabView software was used to monitor and save the data. In addition, the Engineering Equation Solver was adopted to obtain fluid properties and help carry out all calculations. A Phantom Miro-C210, high-resolution and high-speed camera mounted on a Huvitz microscope and LED lighting system was used to capture the features of flow patterns inside the test section. The number of images per second and the visualisation resolution of this camera were set at 3500 fps and 512 × 512 pixel, respectively. A water chiller (model Cole-Parmer Polystat) using R134a was used to cool a water-glycol solution. This was used to provide the necessary cooling at the condenser/reservoir and the sub-cooler, see Fig. 3.

2.2. Micro-pin fins test section

Three main materials were used to manufacture the present test section namely Polytetrafluoroethylene (PTFE), Polycarbonate and oxygen-free copper. Both the PTFE and the Polycarbonate were chosen to minimize heat losses. The housing and the bottom plate were made of PTFE, while a clear Polycarbonate sheet was used to fabricate the cover plate. This plate also included inlet/outlet semi-circular manifolds, fluid ports, fluid temperature ports and fluid pressure ports. Heat was supplied to the test section by four cartridge heaters having a total capacity of 700 W. These cartridge heaters were inserted vertically inside the heating block, see Fig. 4(a). The heating block and the heat sink block were made of oxygen-free copper. RS-503–357 thermal paste was applied between these two parts to reduce the thermal resistance. The total height of these two parts was 91.5 mm, which was large enough to enable uniform heat distribution underneath the heat sink. This was assessed by Al-Zaidi et al. [33]. A total number of 207 staggered diamond micro-pin fins were fabricated on a base area of width (W_b) 20 mm and length (L_b) 25 mm, see Fig. 4(b), using a high-precision, micro-milling machine (HERMLE C20U). Inlet and outlet plena having a semi-circular shape were also manufactured in the heat sink. An O-ring was placed between the heat sink and the cover plate for sealing the flow. Five thermocouples were inserted horizontally along the heated length, see Fig. 4(b). These thermocouples were placed, at a depth of 10 mm, at a location of 2.5, 7.5, 12.5, 17.5 and 22.5 mm from the inlet to the pins,

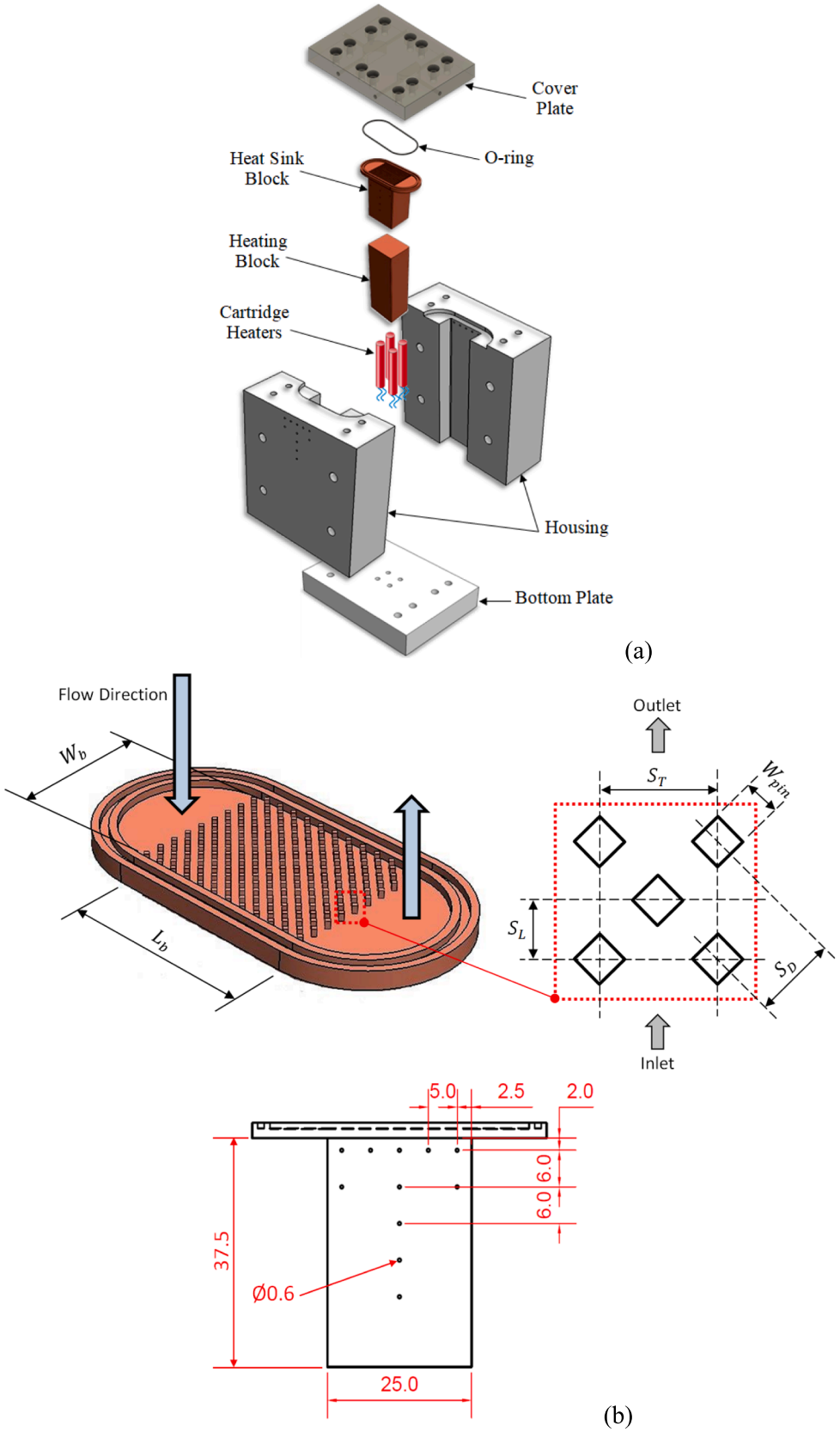

Fig. 4. Experimental test section: (a) exploded drawing of the test section, [4] (b) staggered diamond micro-pin fins heat sink showing locations of the thermocouples (thermocouples were inserted to a depth of 10 mm). Dimensions are in mm.

Table 2
Dimensions of micro-pin fins heat sink.

Symbol	Value [mm]
W_b	20
L_b	25
H_{pin}	1
W_{pin}	0.6
S_T	2.19
S_L	1.095
S_D	1.55
D_h	1.14
$H_{pin}/D_{h,pin}$	1.67

see Fig. 4(b). The vertical distance between these thermocouples and the base of the pins was only 3.5 mm. Table 2 includes the dimensions of this micro-pin fins heat sink. An optical machine ZEISS O-INSPECT having $\pm$ 0.002 mm accuracy was used to measure all these dimensions. 3D Surface Metrology System (NP FLEX) was utilized to measure the surface roughness parameters of the bottom area between pins. Pressurized nitrogen gas was used to initially clean the heat sink and remove any dust and debris from the surface. The surface measurements were then carried out, at a room temperature of approximately 22 °C, at different locations, and the average values were calculated. It was found that the average surface roughness (Ra) was 0.151 μm, while the average surface roughness over the scanned area (Sa) was measured to be 0.114 μm. HFE-7100 is a super-hydrophilic fluid on metallic surfaces. A sessile drop standard method was used to measure the static contact angle of this fluid on copper and aluminium surfaces. Accurate measurements of this angle were challenging, as the droplets spread completely over the surfaces [1]. Li et al. [34] also reported that this fluid has nearly zero contact angle on all types of surfaces.

2.3. Experimental procedure

The system pressure (inlet pressure at the test section) was controlled during the experiments by adjusting the pressure inside the liquid reservoir, see Fig. 3. This was done by controlling the cooling process (via the chiller system) and/or the heating process (via the electric heater immersed in this tank). The required mass flow rate was adjusted using the digital driver mounted to the micro-gear pump. The fluid inlet temperature (and hence degree of inlet sub-cooling) was controlled via the pre-heater. A variable transformer (variac) with a power meter was used to control the supplied heat to the heat sink. Some essential steps were carried out before conducting two-phase flow experiments. Firstly, a de-gassing process was performed to remove any dissolved air from the working fluid. This process was carried out before the commencement of the two-phase flow experiments. The working fluid was boiled in the liquid reservoir for approximately one hour. When the pressure inside the reservoir reached 2 bar, the cooling coil at the top of this reservoir was switched on. This procedure was carried out to ensure that the fluid vapour condensed back into liquid at the bottom of the reservoir, while air was trapped at the top. The trapped air was subsequently vented to the ambient by carefully opening the top-mounted ventilation valve. These steps were repeated until the temperatures of the liquid, vapour and the saturation temperature (corresponding to the reservoir pressure) were the same. After that, adiabatic and diabatic experiments were done to validate the experimental facility. Two-phase flow experiments were then performed at different operating conditions. A set of experiments was repeated after two weeks to ensure the repeatability of our data. In two-phase flow experiments, the mass flux ranged from 100 to 250 kg/m^2 s, while the base heat flux was varied from 12 to 630 kW/m^2. The inlet pressure was 1, 1.5 and 2 bar and the inlet degree of sub-cooling was kept at 5 K. The corresponding wall heat flux varied up to 324 kW/m^2 (or up to exit vapour quality near one). HFE-7100 was chosen as the working fluid due to its dielectric and eco-friendly properties. This refrigerant is also recommended for cooling most electronics since its saturation temperature is 61 °C at atmospheric pressure. The maximum thermal limit at each operating condition was assessed, keeping the heat sink base temperature below 100 °C, i.e. an acceptable limit for most electronics. The thermophysical properties of HFE-7100, for this range of pressures and operating conditions, are summarised in Table 3.

3. Data reduction and validation

3.1. Single-phase experiments

The single-phase Fanning friction factor of the pin–fin heat sink (length of 25 mm in the flow direction in the present design) is calculated from Eq. (9), see Falsetti et al. [18].

$$f = \frac{\Delta P_{pin}\rho_l D_h}{2G_{ch}^2 L_b} \tag{9}$$

The pressure drop of the pin–fin heat sink is calculated as follows:

$$\Delta P_{pin} = \Delta P_{meas} - \left(\Delta P_{sc,sp} + \Delta P_{se,sp}\right) \tag{10}$$

$$\Delta P_{sc,sp} = \left[1 - \left(\frac{H_{pin}W_{ch}N_{ch}}{H_{pin}W_b}\right)^2 + K_c\right]\frac{G_{ch}^2}{2\rho_l} \tag{11}$$

$$\Delta P_{se,sp} = \frac{K_e G_{ch}^2}{2\rho_{l,o}} \tag{12}$$

$$K_c = 0.0088\left(\frac{H_{pin}}{W_{ch}}\right)^2 - 0.1785\left(\frac{H_{pin}}{W_{ch}}\right) + 1.6027 \tag{13}$$

$$K_e = -2 \times 1.33\left(\frac{H_{pin}W_{ch}N_{ch}}{H_{pin}W_b}\right)\left[1 - \left(\frac{H_{pin}W_{ch}N_{ch}}{H_{pin}W_b}\right)\right] \tag{14}$$

The total measured pressure drop ΔP_{meas} was found from the differential pressure drop transducer. The channel hydraulic diameter and mass flux can be found from Eq. (15) and (16) by using the number of channels N_{ch} between pin lines [18].

$$D_h = \frac{4(H_{pin}W_{ch})}{(2H_{pin} + 2W_{ch})} \tag{15}$$

$$G_{ch} = \frac{\dot{m}}{H_{pin}W_{ch}N_{ch}} \tag{16}$$

(Note: the end between the first and last column of pins and the casing of the heat sink is included as a channel, i.e. two additional channels).

The local heat transfer coefficient in single-phase along the heated length is found from Eq. (17), while the average heat transfer coefficient is calculated from Eq. (18).

Table 3
Thermophysical properties of HFE-7100 at the examined operating conditions.

P_i[bar]	T_{sat}[°C]	ρ_l[kg/m^3]	ρ_g[kg/m^3]	i_{lg}[J/kg]	cp_l[J/kg K]	cp_g[J/kg K]	μ_l[μPa s]	μ_g[μPa s]	k_l[W/m K]	k_g[W/m K]	σ[N/m]
1	60.67	1420	9.58	115,663	1177	937.2	393.7	19.84	0.06185	0.00859	0.0096
1.5	73.35	1383	14.13	111,292	1194	969.4	341.6	20.62	0.05938	0.00929	0.0085
2	83.08	1353	18.66	107,811	1211	995.6	312.2	21.22	0.05747	0.00983	0.0077

Table 4
Experimental uncertainties.

Variables	Uncertainty
Temperature	±0.21 − 0.6 K
Pressure	±0.25 %
Mass flow rate	±0.035 %
Fanning friction factor	up to ± 11 %
Reynolds number	±0.94 %
Average Nusselt number	up to ± 13 %
Wall heat flux	±0.66–17 %
Average two-phase heat transfer coefficient	±0.6–16 %

$$h_{(z)} = \frac{q_w^{''}}{(T_{w(z)} - T_{l(z)})} \tag{17}$$

$$\overline{h} = \frac{1}{L_b}\int_0^{L_b} h_{(z)} dz \tag{18}$$

The average Nusselt number is then calculated as follows:

$$Nu = \frac{\overline{h} D_h}{k_l} \tag{19}$$

The wall heat flux $q_w^{''}$ is found from the base heat flux $q_b^{''}$ that is obtained from the vertical temperature gradient of the thermocouples seen in the block under the heat sink of Fig. 4(b).

$$q_w^{''} = q_b^{''} \frac{A_b}{A_{ht}} \tag{20}$$

where

$$q_b^{''} = k_{cu} \left.\frac{dT}{dy}\right|_{y=0} \tag{21}$$

The base area A_b is 20 mm × 25 mm, while the total heat transfer area A_{ht} is calculated from Eq. (22) for adiabatic fin tips with a fin efficiency given by Eq. (23).

$$A_{ht} = A_b - N_{pin} W_{pin}^2 + 4 N_{pin} \eta_{pin} H_{pin} W_{pin} + 2 H_{pin} L_b \tag{22}$$

$$\eta_{pin} = \frac{tanh(m H_{pin})}{m H_{pin}} \tag{23}$$

where

$$m = \sqrt{\frac{4 h_{(z)}}{k_{cu} W_{pin}}} \tag{24}$$

Eq. (25) is used to calculate the local wall surface temperature $T_{w(z)}$, while the local liquid temperature $T_{l(z)}$ is found from Eq. (26).

$$T_{w(z)} = T_{th(z)} - \frac{q_b^{''} Y}{k_{cu}} \tag{25}$$

$$T_{l(z)} = T_{l,i} + \frac{q_b^{''} W_b z}{\dot{m} c p_l} \tag{26}$$

The local temperature $T_{th(z)}$ was recorded by the K-type thermocouples placed underneath the pins, see Fig. 4(b). The inlet liquid temperature $T_{l,i}$ was recorded by the T-type thermocouple placed at the inlet of the heat sink.

3.2. Two-phase experiments

In flow boiling experiments, the two-phase pressure drop is found from Eq. (27).

$$\Delta P_{tp} = \Delta P_{pin} - \Delta P_{sp} \tag{27}$$

$$\Delta P_{sp} = \frac{2 f_{sp} G_{ch}^2 L_{sub}}{\rho_l D_h} \tag{28}$$

A Fanning friction factor is required in Eq. (28). This can be found by fitting the present adiabatic data for laminar flow as a function of the Reynolds number, see Section 3.3 below.

$$f_{sp} = 1.577 Re^{-0.214} \tag{29}$$

The sub-cooled length L_{sub} is calculated from Eq. (30).

$$L_{sub} = \frac{\dot{m} c p_l (T_{sat(z,sub)} - T_{l,i})}{q_b^{''} W_b} \tag{30}$$

The saturation temperature at the sub-cooled region $T_{sat(z,sub)}$ is found from the corresponding local pressure at this region as follows:

$$P_{sat(z,sub)} = P_i - \frac{2 f_{sp} G_{ch}^2 L_{sub}}{\rho_l D_h} \tag{31}$$

The sudden expansion pressure drop in two-phase is calculated using the widely reported expression in the literature [35,36]:

$$\Delta P_{se,tp} = \frac{v_{l,o} + x_o v_{lg,o}}{2}\left(G_p^2 - G_{ch}^2\right) + \frac{(v_{l,o} + x_o v_{lg,o}) G_{ch}^2}{2}\left[1 - \left(\frac{H_{pin} W_{ch} N_{ch}}{H_{pin} W_b}\right)\right]^2 \tag{32}$$

where

$$G_p = \frac{\dot{m}}{H_{pin} W_b} \tag{33}$$

The local two-phase heat transfer coefficient is calculated by replacing the local liquid temperature $T_{l(z)}$ by the local saturation temperature $T_{sat(z)}$, see Eq. (17). The average two-phase heat transfer coefficient is then found as follows:

$$\overline{h}_{tp} = \frac{1}{L_{tp}}\int_{L_{sub}}^{L_b} h_{(z)} dz \tag{34}$$

The local saturation temperature $T_{sat(z)}$ is found from the local pressure in the saturated region as shown in Eq. (35). A linear pressure drop along the axial length was assumed in this calculation.

$$P_{sat(z)} = P_{sat(z,sub)} - \left(\frac{z - L_{sub}}{L_b - L_{sub}}\right)\Delta P_{tp} \tag{35}$$

The local vapour quality can be calculated from Eq. (36).

$$x_{(z)} = \frac{i_{(z)} - i_{l(z)}}{i_{lg(z)}} \tag{36}$$

where

$$i_{(z)} = i_i + \frac{q_b^{''} W_b z}{\dot{m}} \tag{37}$$

The exit vapour quality is calculated at the outlet conditions using Eq. (36). The experimental accuracy of the measured variables is included in Table 4. In the present study, all thermocouples were carefully calibrated using a constant temperature bath (water-glycol) and a precision thermometer (ASL-F250 MK II). The data were collected at steady conditions, i.e. when the variation in all the recorded signals was less than 5 %. The experimental uncertainty of the calculated variables is also presented in Table 4. These uncertainties were obtained using the following general equation:

$$U_r = \sqrt{\left\{\frac{\partial r}{\partial X_1} U_{X1}\right\}^2 + \left\{\frac{\partial r}{\partial X_2} U_{X2}\right\}^2 + \cdots + \left\{\frac{\partial r}{\partial X_j} U_{Xj}\right\}^2} \tag{38}$$

where X_1, X_2 and X_j are the measured parameters with the uncertainties of U_{X1}, U_{X2} and U_{Xj}. This method is described in detail in Coleman and

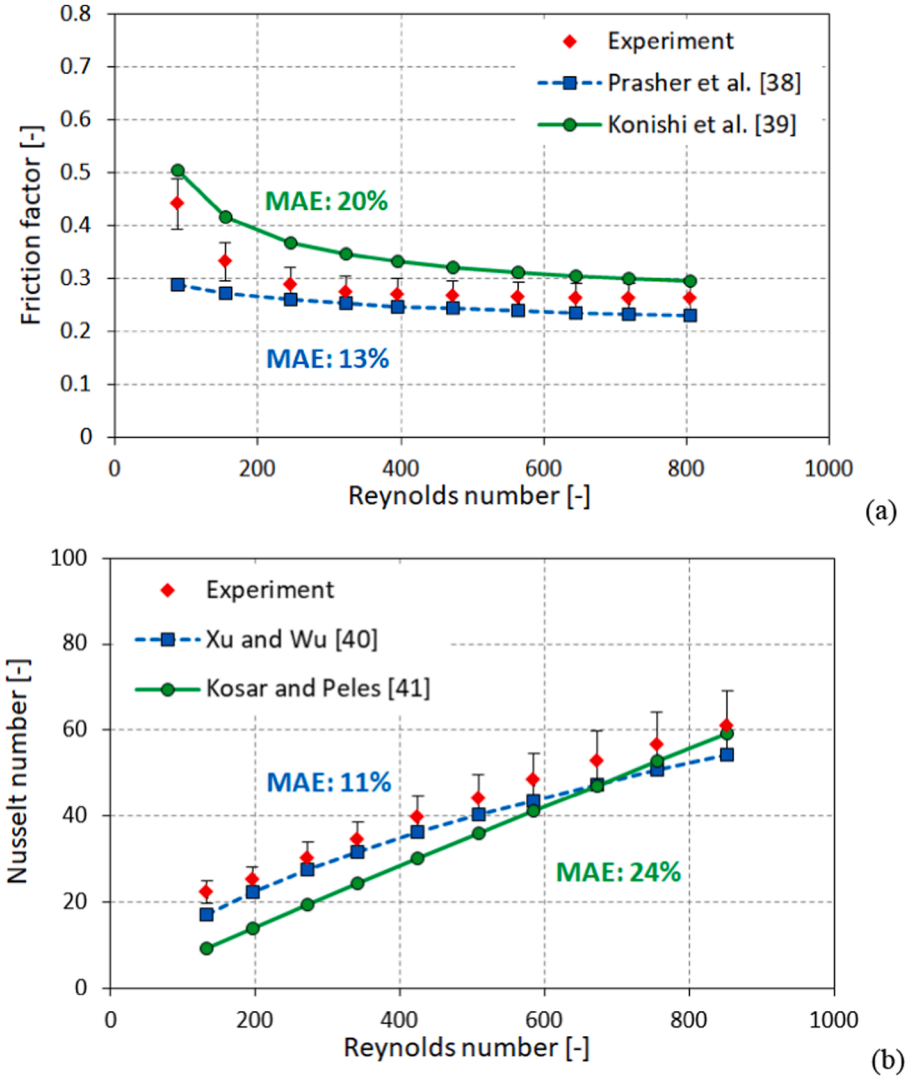

Fig. 5. Single-phase flow validation: (a) friction factor Eq. (9) and (b) Nusselt number Eq. (19).

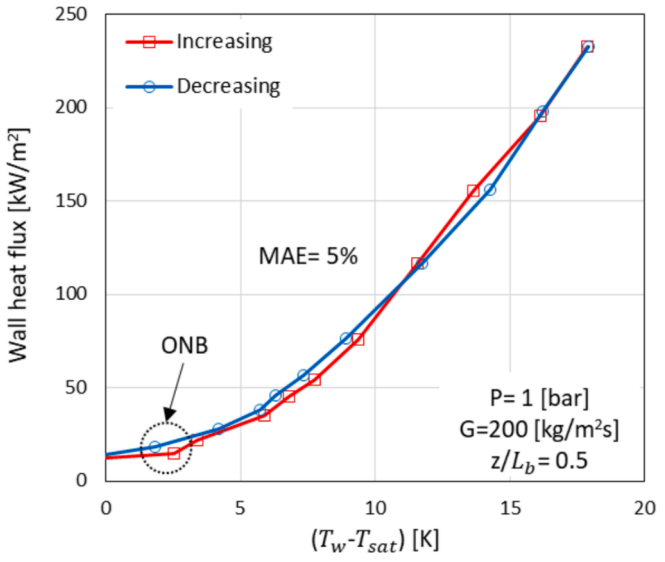

Fig. 6. Effect of hysteresis on the boiling curve of HFE-7100.

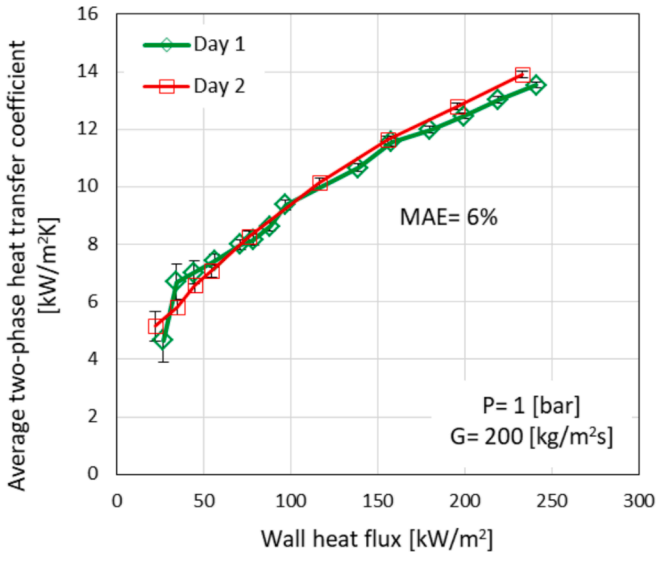

Fig. 7. Repeatability after two weeks of first experiments.

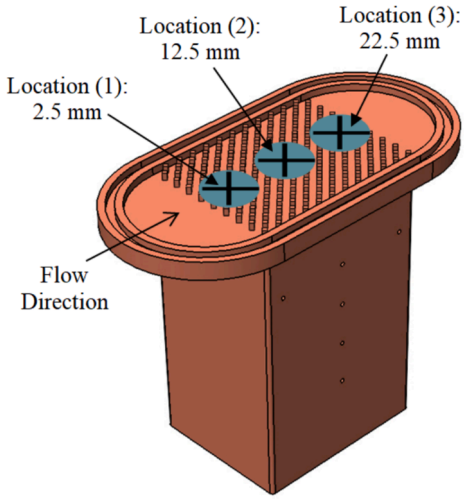

Fig. 8. Visualisation locations with the high-speed, high-resolution camera along the heat sink at 512 × 512 pixels and 3500 fps. Location distance is measured from the channel inlet.

Steele [37]. The mean absolute error is used to assess the existing correlations and is obtained as follows:

$$MAE = \frac{1}{N}\sum \left| \frac{f_{pred} - f_{exp}}{f_{exp}} \right| 100\% \tag{39}$$

where N is the number of data points.

3.3. Single-phase validation

Adiabatic and diabatic experiments were conducted before the two-phase flow experiments. The friction factor and the average Nusselt number versus the Reynolds number were calculated and compared with some existing correlations as shown in Fig. 5. It is important to clarify that these correlations included the maximum mass flux and the hydraulic diameter of the pin cross-sectional area. Therefore, these two parameters were used in this comparison. Fig. 5(a) depicts that the friction factor decreased with increasing Reynolds number as expected. It can also be seen that the staggered pins correlations by Prasher et al. [38] and Konishi et al. [39] predicted the results well with a MAE of 13 % and 20 %, respectively. The experimental results were correlated to produce the single-phase friction factor and *Re* number relation of equation (29) by following the procedure described in Section 3.1 and 3.2.

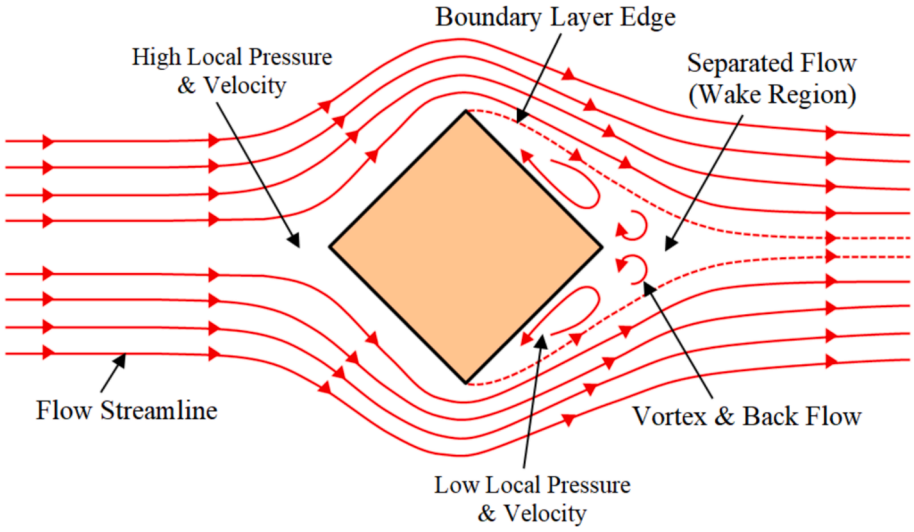

Fig. 9. Schematic diagram of flow regions at the upstream and downstream side of a single pin.

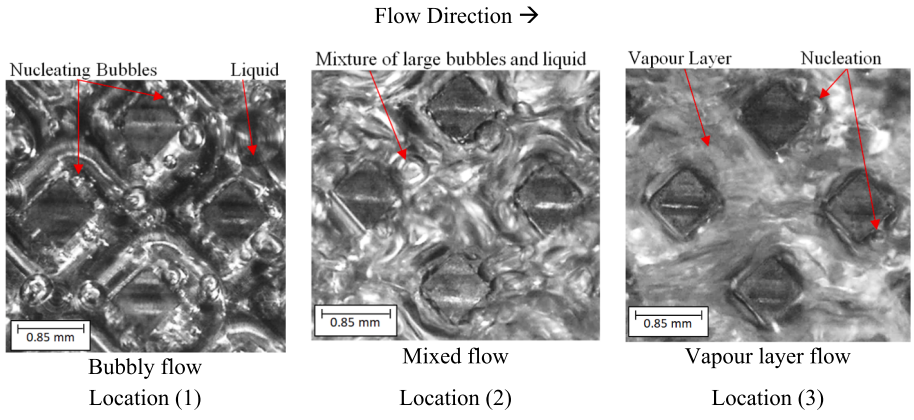

Fig. 10. Experimental flow patterns along the heat sink at 1 bar pressure, 100 kg/m^2 s mass flux and 47 kW/m^2 wall heat flux.

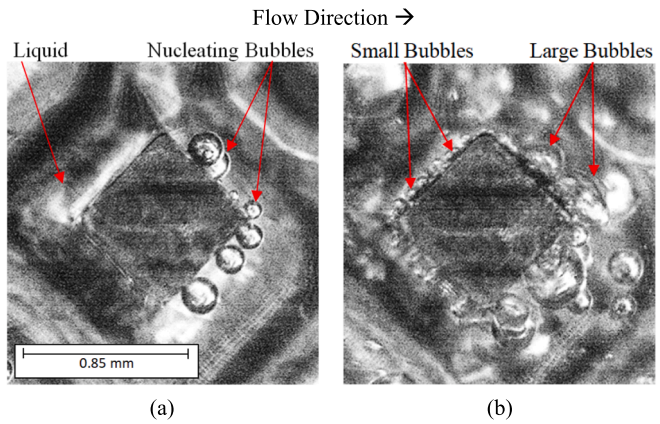

Fig. 11. Nucleation around one pin at the location (1), 1 bar pressure, 250 kg/m^2 s mass flux and wall heat flux of: (a) 42 kW/m^2 (b) 68 kW/m^2.

Fig. 5(b) shows that the average Nusselt number increased with the Reynolds number as a normal trend. It also depicts that the present results were predicted very well by the correlation of Xu and Wu [40] with a MAE of 11 %, and the correlation of Kosar and Peles [41] with a MAE of 24 %. It is worth mentioning that the correlation by [40] was proposed for staggered diamond pins, which is similar to the present geometry and arrangement. It can be concluded from the above that the single-phase results were validated and the experimental facility can be used to conduct high-accuracy two-phase flow experiments.

3.4. Hysteresis and reproducibility of results

Thermal stability is an important design criterion that should be considered in the thermal design of cooling systems for electronics. It is well-known that the performance of any electronic chip can vary during operation. This can result in a variation of required thermal dissipation, i.e. increasing or decreasing. At the same time the results for increasing and decreasing heat flux can differ in pool or flow boiling due to the hysteresis effect. Therefore, the hysteresis effect was examined in this study by increasing and then decreasing the supplied power to the heat sink via the cartridge heaters. Fig. 6 shows increasing and decreasing wall heat fluxes at 1 bar system pressure and mass flux of 200 kg/m^2 s. It is clear that both trends were close to each other with a mean absolute difference of only 5 %. This shows that the hysteresis effect was negligible at these operating conditions. The wall heat flux examined in this figure was varied from 6 to 233 kW/m^2.

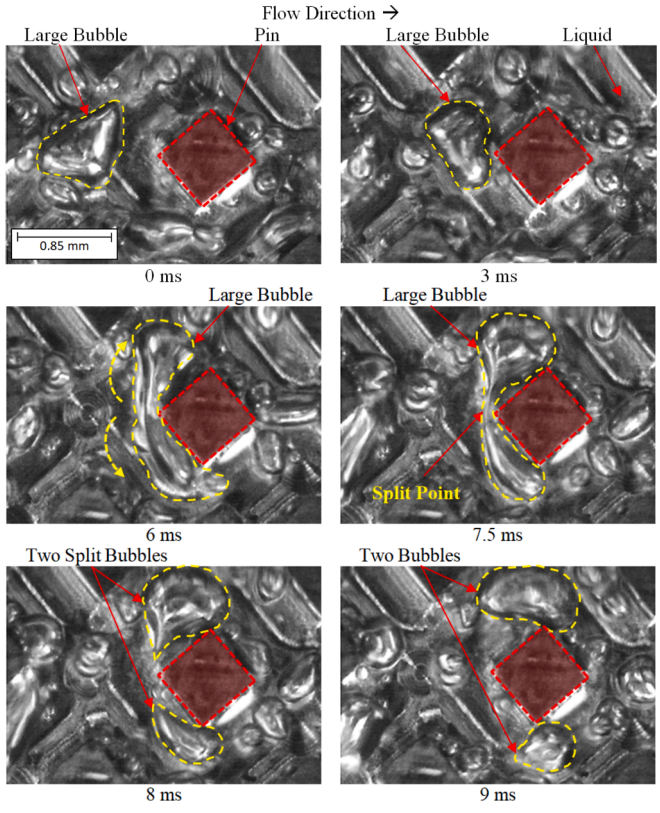

Fig. 12. Sequence of images of the bubble separation at the location (2), 1 bar pressure, 200 kg/m^2 s mass flux and 27 kW/m^2 wall heat flux.

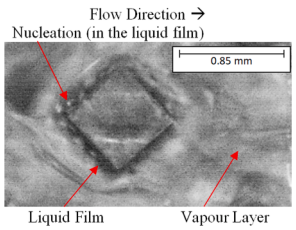

Fig. 13. Vapour layer flow with nucleation in the liquid film around one pin at the location (3), 2 bar pressure, 200 kg/m^2 s mass flux and 74 kW/m^2 wall heat flux.

The reproducibility of the results was also examined to assess the repeatability and reliability of our experimental results. Two complete sets of experiments were repeated with two weeks between them, as shown in Fig. 7. This figure depicts that the two-phase heat transfer results were repeatable with a MAE of 6 %. The operating conditions shown in this figure were at 1 bar inlet pressure, mass flux of 200 kg/m^2 s and wall heat flux up to 240 kW/m^2. These results also confirm that the surface condition was not affected by the boiling process for these particular test periods described in this paper. A specific study will need to be carried out aimed at evaluating the surface condition and possible ageing over longer testing periods.

4. Results and discussion

4.1. Flow boiling patterns

The clear understanding of the prevailing of flow patterns during boiling experiments is a fundamental and crucial step to clarify the heat transfer mechanism(s) in micro-scale systems. Therefore, these features were captured and studied in detail in this study. The high-speed, high-resolution camera was focussed at different locations along the heat sink as shown in Fig. 8. The basic flow structure around a pin is sketched in Fig. 9. This figure is presented here to explain the following experimental features of flow patterns. It depicts that, at the pin upstream, there is a high velocity and pressure region. In contrast, downstream of the pin there is a region of low velocity and pressure, which included flow separation and recirculation. Boundary layer formation begins at the sharp edge of the pin as shown in this figure, although flow recirculation tends to disrupt this tendency, especially at high velocities. Different flow features around pins and the effect of operating conditions are discussed in the next sections.

4.1.1. Flow patterns across the entire heat sink

The experimental flow patterns along the entire heat sink are presented in Fig. 10. In our study, three flow patterns were classified as shown in this figure: (i) Bubbly flow with clear small nucleating bubbles in the liquid flow was captured at location (1). At this location, nucleation was seen around the pin perimeter. (ii) Mixed flow characterised by large vapour bubbles mixing with liquid flow was seen at location (2). Nucleation was also seen around the pins. (iii) Vapour flow on the bottom surface and around the pins was observed at location (3). A

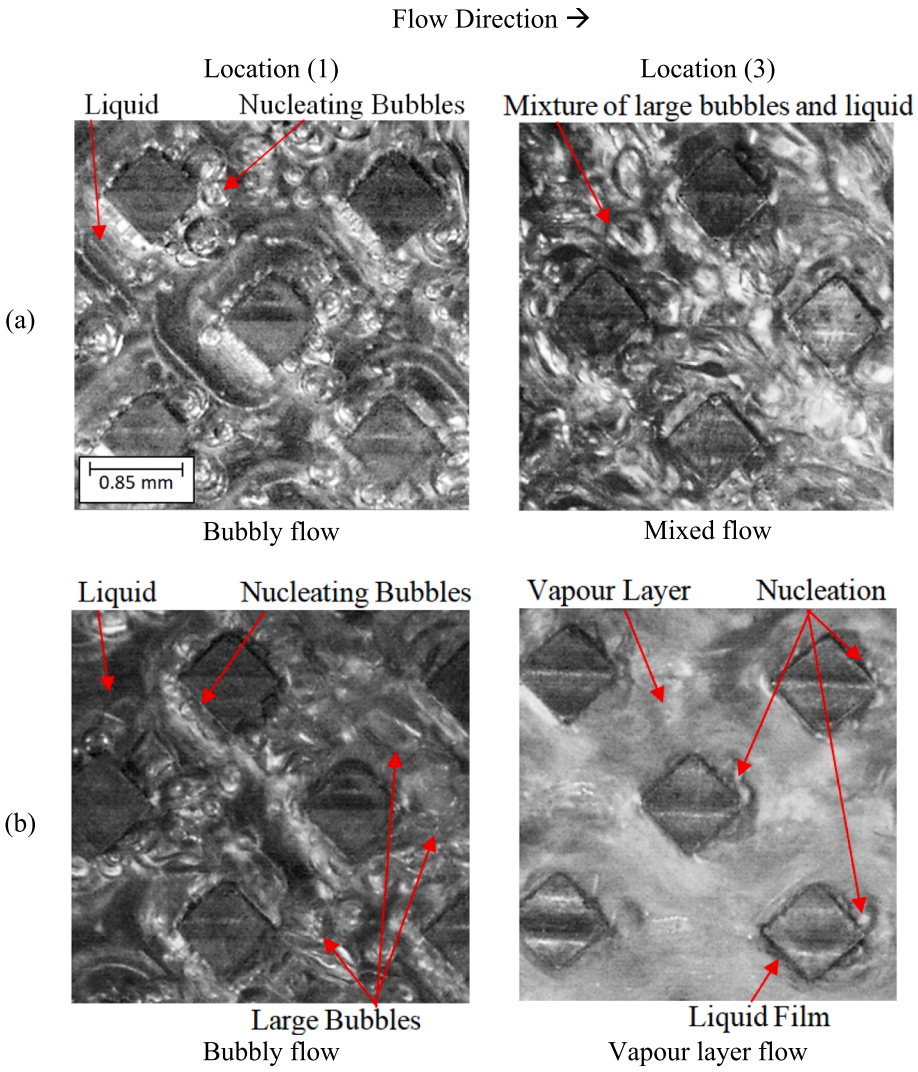

Fig. 14. Effect of heat flux at 1 bar pressure and 200 kg/m^2 s mass flux: (a) 78 kW/m^2 (b) 138.7 kW/m^2.

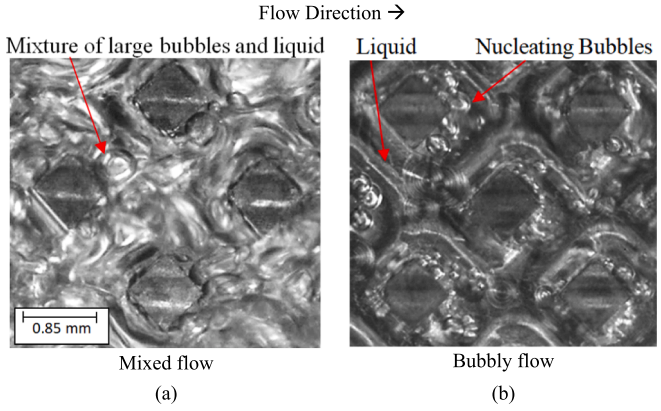

Fig. 15. Effect of mass flux at the location (2), 1 bar pressure and 47 kW/m^2 wall heat flux: (a) 100 kg/m^2 s (b) 250 kg/m^2 s.

liquid film was also seen to exist around the pins during this flow pattern. Bubble nucleation was seen to occur in the liquid film on close observation. The resulting flow patterns are mostly due to pressure changes along the flow direction as well as in-between pins and bubble coalescence. Nucleation process can clearly be seen in all these flow regimes.

4.1.2. *Differences between the upstream and downstream side of the pin*

Different features of flow patterns in micro-pin fin heat exchangers were reported in the literature, see [13,20,42,43]. However, the differences in bubble nucleation, bubble sizes and flow patterns at the upstream and downstream sides of pins were not specifically discussed. Therefore, we present below a detailed analysis on these different observations at the upstream and downstream sides of the pins. Different features of flow patterns were seen around pins due to the fact that the local velocity and pressure at the upstream and downstream side of the pins are not the same. The camera was focussed on a single pin to capture these features at a wide range of operating conditions. Fig. 11 shows the nucleation process around a single pin at a system pressure of 1 bar, mass flux of 250 kg/m^2 s and two different wall heat fluxes. These images were taken at location (1), i.e. near the heat sink inlet. It is clear that, at low heat flux of 42 kW/m^2, the nucleation first started at the downstream side of the pin, while the upstream side is still not active. As mentioned above, the downstream side is at a lower pressure that can easily trigger nucleation, i.e. this depressurising region results in phase change due partly to flashing and bubble nucleation with bubbles that remain on the surface and have time to grow in the lower velocity region. When the wall heat flux increased to 68 kW/m^2, bubble nucleation occurs at the upstream side as well. It is also interesting to note that the nucleating bubbles at the upstream side had smaller diameter than those

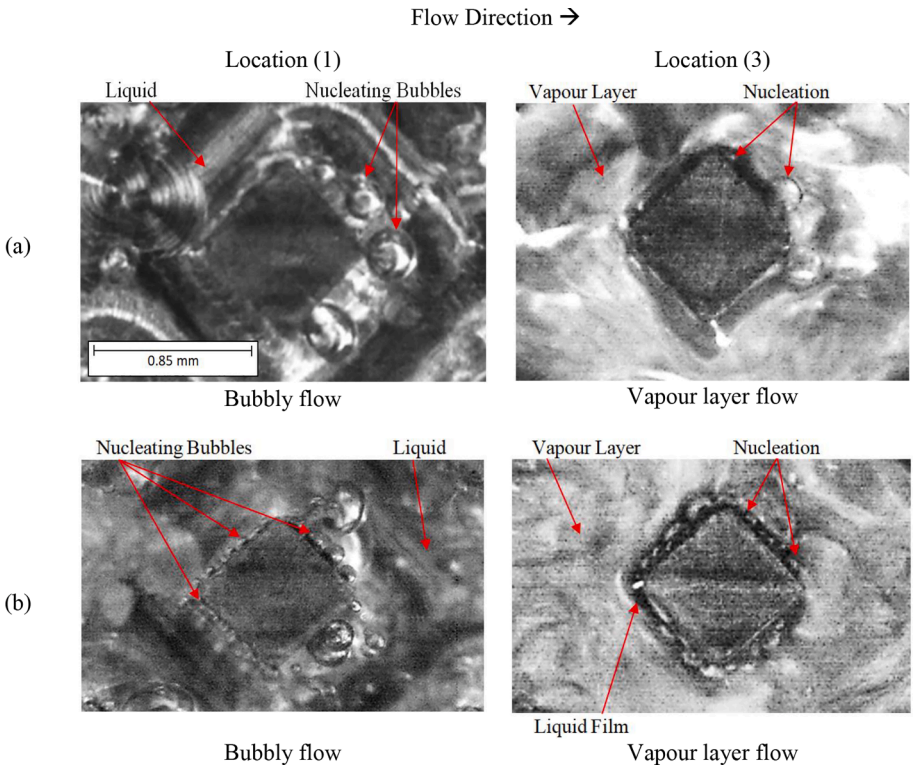

Fig. 16. Effect of system pressure at 100 kg/m^2 s mass flux and 58 kW/m^2 wall heat flux: (a) 1 bar (b) 2 bar.

at the downstream side of the pin. This could be due to the fact that there is higher local pressure at the upstream and hence smaller surface tension, i.e. smaller bubbles. Larger bubbles at lower pressure were also reported and explained in the pool boiling work of [44]. In addition, the high flow velocity at the upstream results in a high inertia force that could strip bubbles away from their nucleation sites, i.e. not enough time for bubble growth resulting in smaller departing bubbles. It is also clear that the nucleating bubbles occur around the edge of the pin and the bottom surface, while the surface area between pins is still not active at these operating conditions. This edge having an angle with the bottom surface is at a higher temperature than the rest of the pin and can more easily trap the vapour and help initiate bubble generation. In addition, the nucleating bubbles at the downstream pin side remain at the pin edge and then slide and coalesce with others bubbles increasing in size. Some of these bubbles tend to move towards the upstream pin corners. This bubble movement could be due to the circulatory back flow in the downstream wake. When these bubbles reach the pin corners, they are carried away by the incoming fluid and depart in the mainstream flow. The bubbles generated at the upstream pin side can easily slide and coalesce, while continuing to travel along the pin edge departing at the pin corner.

Another feature captured during flow visualisation showed that large bubbles could impinge on a downstream pin and break up. This is seen in the images captured with the camera at location (2), see Fig. 12. The pin was shaded with a red area to easily identify the corners of this pin. At 0 ms, a large bubble can be seen traveling towards this pin, see the yellow dashed line. At 3 ms, this large bubble touches the pin corner and continues to move around the pin at 6 ms. Between 7.5 and 8 ms, the bubble is split in two and travels at the sides of the pin. At 9 ms, these two bubbles were captured to travel in the main stream flow. It is therefore clear that the staggered pin fin arrangement is able to split large bubbles, which were then seen to merge with other bubbles downstream and move in a zig-zag path. This verifies the effect of pin geometrical arrangement in the heat sink on both flow patterns and subsequently heat transfer rates and pressure drop. Examination of the bubble movement at this location and these parametric conditions, indicated no back flow or flow reversal.

Fig. 13 depicts a close image of vapour layer flow around a single pin at location (3), system pressure of 2 bar, mass flux of 200 kg/m^2 s and wall heat flux of 74 kW/m^2. As seen in the figure, a vapour layer forms and surrounds the pin with the existence of a clear liquid film around this pin. Nucleating bubbles also appear in this film and could depart from their nucleation sites. These flow features were visualised in all present experiments. Pins surrounded by liquid film were also captured by Kosar and Peles [13] for R-123 in staggered hydrofoil pins and Law et al. [42] for FC-72 in in-line oblique pins. Markal et al. [43] presented a very clear flow visualisation of flow boiling of de-ionized water using in-line square pins, and a liquid film around pins with nucleation sites was captured.

4.1.3. *Effect of heat flux*

The effect of wall heat flux on the prevailing flow patterns is shown in Fig. 14. This figure was captured at location (1) and (3), at a system pressure of 1 bar and mass flux of 200 kg/m^2 s. At location (1), bubbly flow was captured when the heat flux was 78 kW/m^2. Most of these bubbles occur at the pin edges, while few nucleating bubbles were captured on the bottom surface. Bubbly flow was still seen when the heat flux increased to 138.7 kW/m^2. However, some large bubbles, i.e. larger than those at the lower heat flux, occur between pins. The bottom surface between these pin becomes more active at this heat flux. High bubble generation and coalescence rate could lead to the formation of these large bubbles with increasing heat flux, i.e. increasing wall surface temperature. When the camera was moved to location (3), mixed flow was seen at 78 kW/m^2, while vapour flow was captured at the higher heat flux of 138.7 kW/m^2. The nucleation process can still be seen in these flow regimes, i.e. in mixed and vapour flow, indicative of its possible partial contribution to the heat transfer rates.

4.1.4. *Effect of mass flux*

Two mass fluxes of 100 and 250 kg/m^2 s were selected to study the

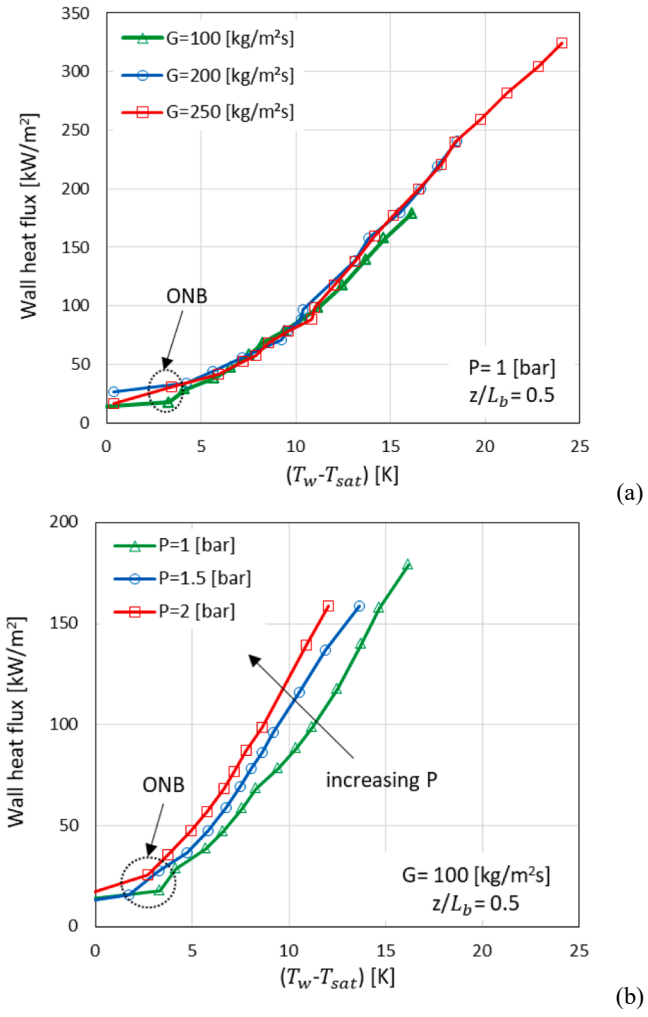

Fig. 17. Experimental boiling curve of HFE-7100 at different operating conditions: (a) Mass flux effect (b) System pressure effect.

effect of this parameter at 1 bar system pressure and wall heat flux of 47 kW/m^2 as shown in Fig. 15. At the lower mass flux, mixed flow was visualised at location (2). However, bubbly flow was seen at the higher mass flux. It is well known that, for a given heat flux, increasing mass flux leads to a reduction of the thermal boundary layer on the surface. This could reduce the bubble generation and coalescence rate and then delay the appearance of subsequent flow patterns.

4.1.5. *Effect of system pressure*

The effect of system pressure on the observed flow pattern features is depicted in Fig. 16. This figure is presented at a mass flux of 100 kg/m^2 s, wall heat flux of 58 kW/m^2 and inlet pressure of 1 and 2 bar. Two locations, near the heat sink inlet and the outlet, were selected to capture these flow features. At location (1), nucleating bubbles were seen for these two inlet pressures. However, the features of these bubbles are not the same. For example, at a system pressure of 1 bar, a small number of large bubbles were captured at the downstream side of the pin, while there is no nucleation seen at the upstream side. When the pressure increased to 2 bar, a larger number of smaller bubbles can be seen around the pin, i.e. nucleation occurred also at the upstream side. The upstream bubbles were smaller in size than the ones nucleating and growing at the downstream side. High system pressure results in smaller surface tension promoting smaller bubble sizes [44]. The effect of system pressure on the features of vapour flow can be seen towards the exit of the heat sink, see location (3). It is clear that although a vapour layer occurs on the surface for both pressures, more nucleation sites in the liquid film around the pins were found with increasing pressure. From the flow visualisation results we can also deduce that the liquid film around these pins becomes thicker at higher system pressure. However, it was difficult to measure and compare the thickness of this liquid film during the experiments. Higher system pressure leads to a reduction in the vapour superficial velocity (larger vapour density) and then lower interfacial shear stress. This could then lead to a reduction in the amount of liquid that is removed from the surface resulting in thicker liquid film. The existence of thicker liquid film can then promote higher bubble nucleation activity.

It can be summarised from the above discussion that the geometry of the pin fin heat sink can have a significant effect on the features of flow patterns, which also vary with location along the heat sink. This can then go a long way to explain the differences in pressure drop and heat transfer results seen in the literature, leading to discrepancies among reported data and proposed correlations. The pin geometry as well as the pin arrangement should be considered carefully in thermal-fluid design. The effect of pressure on the prevailing flow features was also clearly seen in the results described here.

4.2. *Experimental boiling curve*

The present boiling curve of HFE-7100 is plotted in Fig. 17 at different operating conditions captured at a location half-way along the heat sink. It can be seen that the wall heat flux increased with increasing temperature difference at all operating conditions, i.e. mass flux of 100, 200 and 250 kg/m^2 s. This figure also shows that the onset of nucleate boiling (ONB) occurred at around 4 K. The mass flux effect on the boiling curve was found to be negligible, see Fig. 17(a). However, it is interesting to know that the operational conditions were extended at the mass flux of 250 kg/m^2 s. The maximum wall heat flux reached 324 kW/m^2, providing a base heat flux of 0.63 MW/m^2, i.e. thermal design power of 315 W at a surface temperature of 84 °C. With reference to published results in Table 1, one can observe that higher base heat fluxes have been reported. However, it is important to note that these were obtained for water or in the case, of refrigerants, with a significantly high degree of sub-cooling, much higher mass fluxes, higher resulting substrate temperatures, and in certain cases more complex or difficult to machine designs. As mentioned above in this paper, in the case of high degree of sub-cooling, the substrate (chip) to be cooled is not at a uniform temperature due to the larger part of the working fluid being in single-phase. This temperature variation in the case of electronic chips requiring cooling plus high temperatures, as in some of the results of Table 1, are detrimental to their operation and longevity. To the best of our knowledge, this is the maximum value reported in the literature at these low operating conditions, i.e. low inlet sub-cooling, atmospheric working pressure and low mass flux, using this refrigerant. It is worth noting that this high heat flux was achieved without the occurrence of dryout regions or approaching critical heat flux conditions. This maximum heat flux reported in the paper was reached at an exit vapour quality close to one. Fig. 17(a) shows that the wall heat flux and temperature difference covered in the present two-phase experiments varied from 15 to 324 kW/m^2 and from 4 to 24 K, respectively.

The effect of system pressure on the boiling curve is shown in Fig. 17 (b). This figure covered a wall heat flux of 15–180 kW/m^2 and temperature difference of 3–16 K. The figure demonstrates that the wall heat flux increased with increasing system pressure, for the temperature difference covered in the results. This effect can be explained based on the previous discussion of Section 4.1 on flow visualisation, i.e. it has been noted that the number of nucleation sites increases with increasing system (inlet) pressure within the range studied. However, this effect could vary at higher pressure ranges, and therefore, more studies should be carried out to verify this effect.

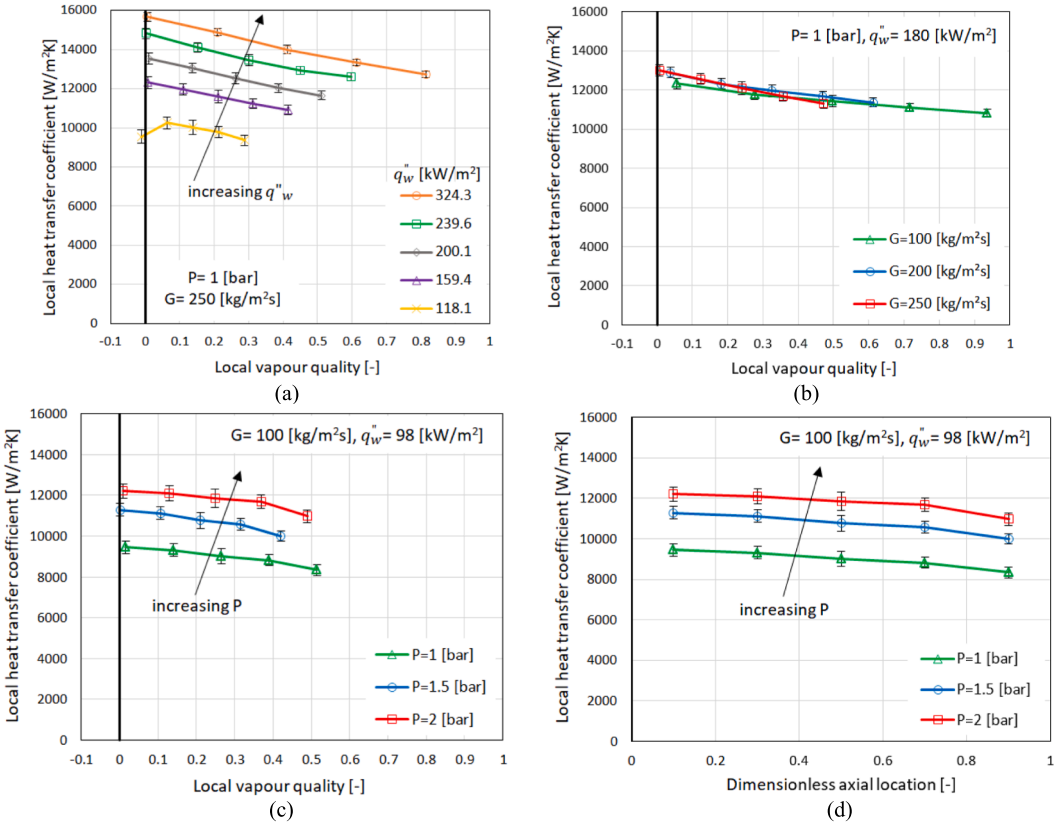

Fig. 18. Local heat transfer coefficient along the heat sink: (a) heat flux effect (b) mass flux effect (c) system pressure effect and (d) HTC versus the axial location.

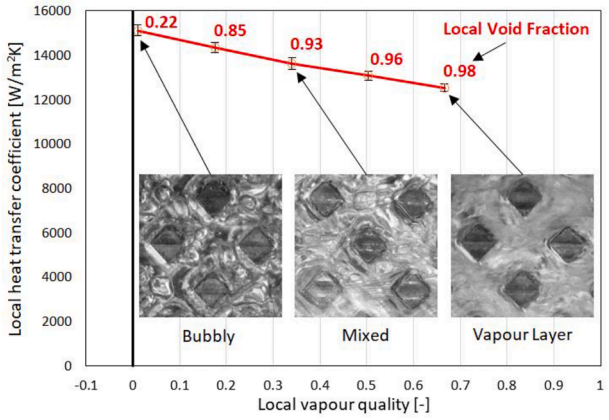

Fig. 19. Local heat transfer coefficient versus local vapour quality, corresponding to the local flow visualisation and local void fraction, at 1 bar system pressure, 260 kW/m^2 wall heat flux and 250 kg/m^2 s mass flux.

4.3. *Two-phase heat transfer coefficient and comparison with correlations*

The local heat transfer coefficient obtained using Eq. (17) versus the local vapour quality is depicted Fig. 18 as a function of heat flux, mass flux and system pressure. This figure was plotted along the heated length including the single and two-phase regions. The local vapour quality reported in this figure covered the range 0–0.94. It was found that the local two-phase heat transfer coefficient decreased with increasing local vapour quality as shown in this figure. This could be due to the reduction in the nucleation process along the heated length when different flow patterns occurred as explained in Section 4.1. Fig. 18(a) was plotted at an inlet pressure of 1 bar and mass flux of 250 kg/m^2 s. It shows that the local heat transfer coefficient increased when the wall heat flux increased from 118 to 324 kW/m^2. This is indicative of the increasing activation of nucleation sites with heat flux. The same dependence on vapour quality is seen in flow boiling in microchannels, see [2].

The mass flux effect on the local heat transfer coefficient was examined at 1 bar inlet pressure and wall heat flux of 180 kW/m^2, see Fig. 18(b). It was found to be insignificant for the range of 100–250 kg/m^2 s. Again here, there are commonalities with flow boiling in microchannels, see [33]. The examined system pressure had a clear effect on the local heat transfer coefficient as depicted in Fig. 18(c-d). These figures were plotted at a wall heat flux of 98 kW/m^2, mass flux of 100 kg/m^2 s and three different inlet pressures, i.e. 1, 1.5 and 2 bar. There is a significant increase in the local heat transfer coefficient with pressure, again in common with flow boiling in microchannels, see [2]. The explanation for this is the increase in the number of active nucleation sites with increasing pressure as discussed in Section 4.1.5. The results above confirm that the bubble nucleation mechanism, which provides higher local heat transfer coefficient than other flow patterns, remains present in the entire flow region of the micro-pin fin heat sink.

Fig. 19 is presented here to show the local measurements of the heat transfer coefficient, vapour quality and void fraction corresponding to the flow visualisation along the heat sink. The Zivi correlation [32], given in Eq. (8) of this paper, was used to calculate the local void fraction in this figure, see red numbers. It can be seen that the local two-phase heat transfer coefficient had the highest value at very low local void fraction, i.e. near from the inlet, when the flow pattern was bubbly flow. These local heat transfer coefficients were found to decrease with increasing local void fraction towards the outlet. The flow pattern changed from the bubbly flow to the mixed flow at the middle of the heat sink and then to the vapour layer flow at the outlet. As seen in this figure, the vapour layer flow, at the outlet, had the lowest local two-phase heat transfer coefficient and the highest local void fraction. The change in the features of these flow patterns with a reduction in the nucleation

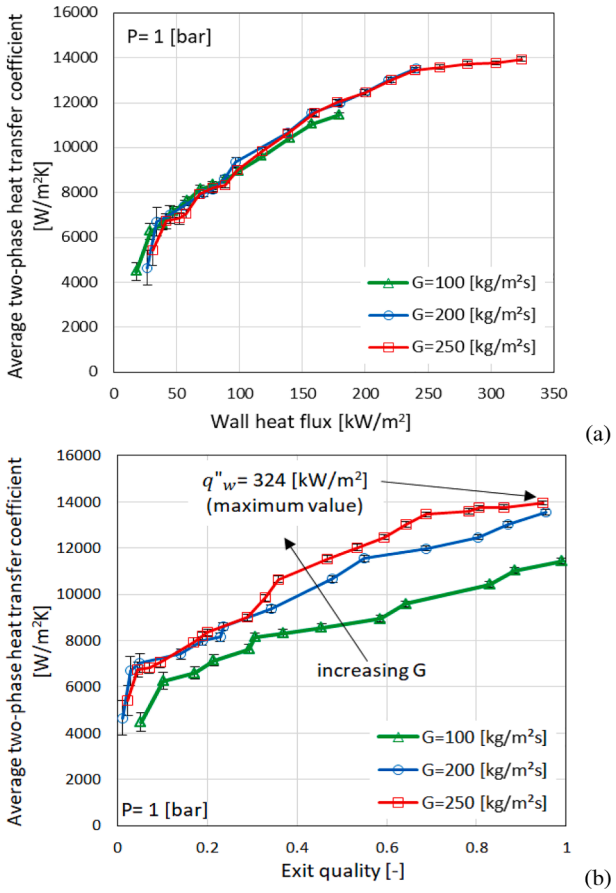

Fig. 20. Average two-phase heat transfer coefficient at different mass fluxes versus: (a) wall heat flux (b) exit vapour quality.

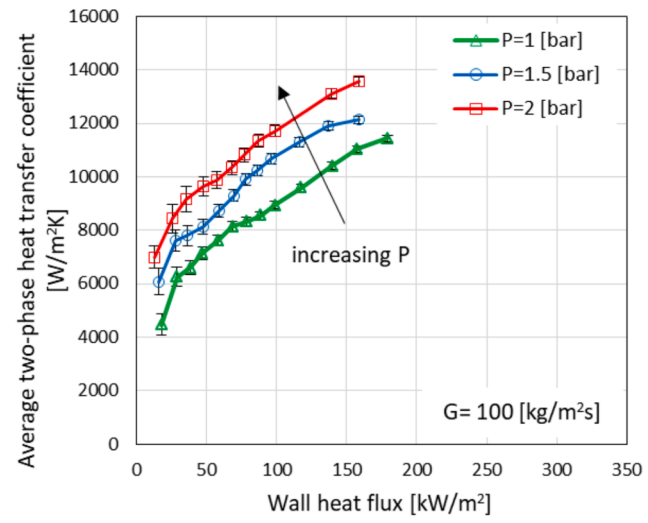

Fig. 21. Average two-phase heat transfer coefficient at different system pressures.

intensity could lead to this local trend in the heat rates along the heat sink.

The effect of wall heat flux and mass flux on the average two-phase heat transfer coefficient obtained using equation (34) is presented in Fig. 20. These results were plotted versus wall heat flux and exit vapour quality. It is clear from Fig. 20(a) that increasing wall heat flux from 16 to 324 kW/m^2 leads to increase the average two-phase heat transfer coefficient due, as mentioned above, to the activation of more nucleation sites. In line with Fig. 18(b), Fig. 20(a) depicts that the effect of mass flux was insignificant. However, when the average two-phase heat transfer coefficient versus the exit vapour quality was plotted, a different heat transfer trend can be seen, as shown in Fig. 20(b). This figure depicts that the average two-phase heat transfer coefficient increased with increasing exit vapour quality and mass flux, which is in contrast to the results reported in Fig. 20(a). It must be noted however, that this is due to the fact that, for a given mass flux, the exit vapour quality increases as the heat flux increases. For a given exit vapour quality, a higher heat flux must be applied as the mass flux increases in order to reach the same exit condition. In other words, the increase in the average two-phase heat transfer coefficient shown in this figure is due to the increase in heat flux. The same trends were reported earlier in Fayyadh et al. [45]. Fig. 20 also illustrates that the average two-phase heat transfer coefficient reached a maximum value of 14,000 W/m^2 K at a wall heat flux of 324 kW/m^2 and mass flux of 250 kg/m^2 s, when the exit vapour quality was around one.

The effect of system pressure on the average two-phase heat transfer coefficient is shown in Fig. 21. Increasing inlet pressure was found to increase the average two-phase heat transfer coefficient. As explained above, increasing system pressure can promote more nucleation around the pins and on the heated bottom surface between the pins. This thermal trend may differ if higher system pressures are tested.

The present heat transfer results were compared with existing correlations proposed for micro-scale pin geometries as presented in Fig. 22. It is interesting to know that the correlation by Cooper [29] for pool boiling was also included in this comparison to evaluate the contribution of the nucleate boiling mechanism. This figure shows that the correlation by Kosar and Peles [13] over predicted the results with a MAE of 89 % although it was proposed for the nucleate boiling mechanism. This could be due to the different pin shape (hydrofoil pins) and fluid properties (R123). However, the pool boiling correlation by Cooper [29] provided the smallest mean absolute error in this comparison, i.e. only 36 %. This can confirm the presence of the nucleate boiling heat transfer mechanism in the present study for all the flow regimes. The convective correlations by Kosar and Peles [13] and Reeser et al. [11] had the highest MAE of 92 % and 98 %, respectively. This large disagreement is expected since a different heat transfer mechanism was found here. The nucleate-convective correlation by Zhuang et al. [24] showed a smaller MAE of 51 % than that proposed by Yubing et al. [16] with a MAE of 59 %. This smaller MAE by [24] compared to [16] could be due to the same working fluid (HFE-7100) used in this correlation.

Fig. 23 was presented here to further evaluate the heat transfer trend of these correlations. This figure was plotted at different wall heat fluxes, inlet pressure of 1 bar and mass flux of 250 kg/m^2 s. It is clear that the nucleate boiling correlations [13,29] and the present results showed an increase in the heat transfer coefficient with increasing heat flux. In contrast, the convective boiling correlations [11,13] provided an opposite trend. The nucleate-convective boiling correlations [16,24] showed an increase and then a reduction in the heat transfer coefficient with increasing heat flux. The contribution of heat transfer mechanisms has a clear effect on these thermal trends. Although these correlations were proposed for the same flow boiling mechanism, a large discrepancy can be seen among them.

The correlation by Yubing et al. [16] was modified here for further assessment of the current heat transfer results. This correlation was selected since it was proposed for staggered diamond pins, and the Cooper correlation was used in their correlation to produce the nucleate boiling component. This pool boiling correlation showed the minimum mean absolute error compared to other flow boiling correlations. Yubing et al. [16] correlated the single-phase heat transfer coefficient based on their experimental data as shown in Appendix I. This parameter was modified here based on the present single-phase flow experiments, i.e. fitting the data presented in Fig. 5 as shown in Eq. (40).

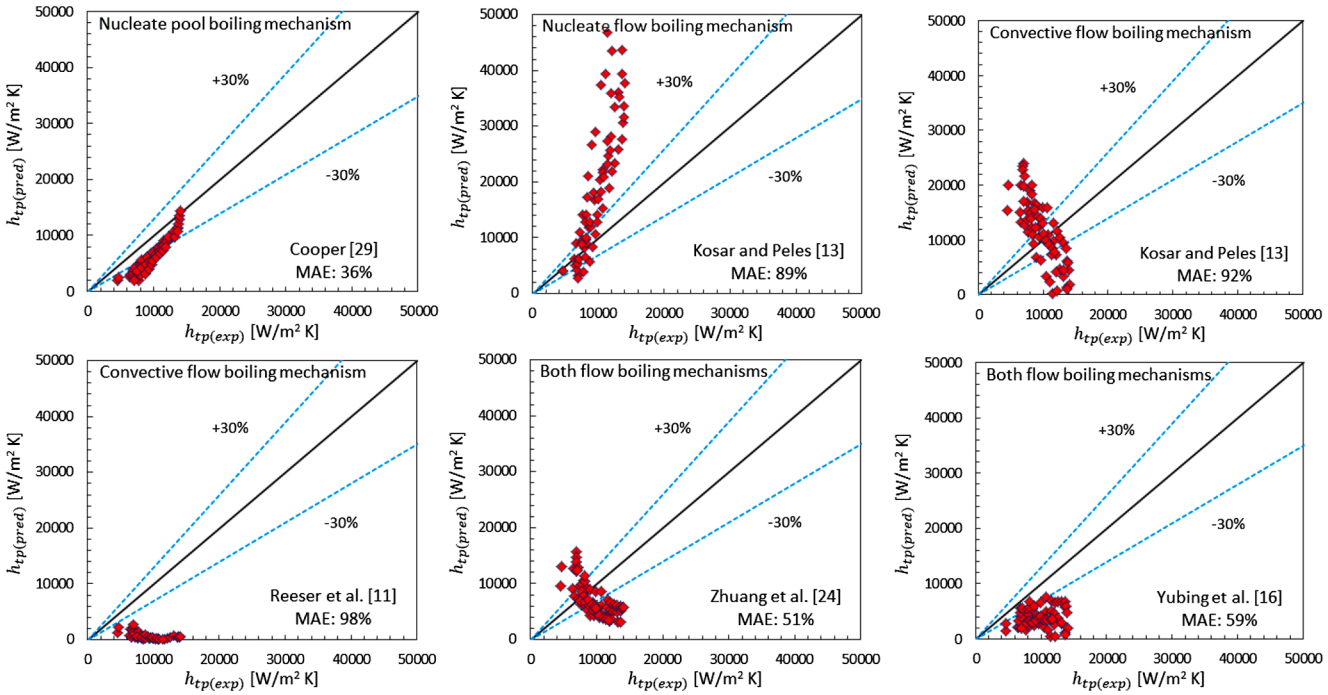

Fig. 22. Two-phase heat transfer comparison with correlations.

$$h_{sp} = 2.5Re^{0.5}\left(\frac{k_l}{D_h}\right) \tag{40}$$

when this modified h_{sp} is used in their correlation, the mean absolute error reduced from 59 % to only 24 %, see Fig. 24(a). The above confirms the importance of nucleate boiling component and the correlation for calculating single-phase heat transfer coefficient as well.

The present heat transfer results showed that both wall heat flux and inlet pressure had a clear effect. Therefore, the Boiling number and the reduced pressure were introduced and plotted in Fig. 24(b). A positive and strong relationship between these two control parameters and the two-phase heat transfer coefficient can be seen in this figure. The present results were also correlated using Eq. (41).

$$h_{tp} = 97618Bo^{0.32}P_R^{0.24} \tag{41}$$

Fig. 24(c) depicts the prediction of this new correlation, with a MAE of 8.8 %, showing the strong dependence of the two-phase heat transfer coefficient on the Boiling number and reduced pressure. This indicates the presence of nucleate boiling mechanism in all the three flow regimes seen in the examined geometry and flow range. It is well-known that nucleation site density, bubble departure diameter and frequency can significantly affect this heat transfer mechanism. In the present study, accurate measurements of these parameters were challenging due to the flow disturbances induced by the pins. This correlation, Eq. (41), presented here is intended only to clarify the dependence on the Boiling number and reduced pressure. It is applicable to the current pin geometry and dimensions, working fluid, inlet sub-cooling of 5 K, inlet pressure of 1–2 bar, mass flux of 100–250 kg/m^2 s and wall heat flux up to 324 kW/m^2.

4.4. Two-phase pressure drop and comparison with correlations

The pressure drop results are also discussed in this paper since this parameter can define the pumping power requirements of the cooling system. Fig. 25 shows the two-phase pressure drop at different exit vapour quality, mass flux and system pressure. It can be seen that the two-phase pressure drop increased with increasing exit quality (heat flux) or mass flux, see Fig. 25(a). This figure covers an inlet pressure of 1, exit vapour quality near one and mass flux of 100, 200 and 250 kg/m^2 s. High acceleration and frictional pressure drop components can lead to this high two-phase pressure drop. This figure also depicts that the maximum two-phase pressure drop was found to be only 18 kPa at the maximum wall heat of 324 kW/m^2 and mass flux of 250 kg/m^2 s. Fig. 25 (b) shows the effect of different system pressures on the two-phase pressure drop at a mass flux of 100 kg/m^2 s. The two-phase pressure drop was found to decrease with increasing system pressure. Lower interfacial shear stress (lower vapour superficial velocity due to the higher vapour density) could reduce the pressure drop components with increasing system pressure.

Four existing two-phase pressure drop correlations were selected and compared with the present results as depicted in Fig. 26. The correlations by Reeser et al. [11] and Zhuang et al. [24] under predicted the data with a MAE of 94 % each. In contrast, the correlations by Li et al. [15] and Xu et al. [17] predicted the present data very well with a MAE of 19.8 % and 22.5 %, respectively. Fig. 27 is plotted to further evaluate the two-phase frictional pressure drop component of these correlations. It is clear that the trend of this component versus the exit vapour quality is the same for these correlations except that by Zhuang et al. [24]. This different trend could be due to the negative exponent in the Lockhart–Martinelli parameter proposed in their correlation. It can be concluded from both Figs. 26 and 27 that (i) correlations having the Chisholm parameter as an empirical constant over predicted the results. This could not work well for different fluid(s), operating conditions and dimensions, i.e. these correlations can only work well within their data range. (ii) Correlations having pin dimensions and space between pins, e.g. fin density and aspect ratio of pin, provided better agreement. Pin dimensions and space should be considered in the two-phase friction multiplier. It is interesting to mention that the correlation by Li et al. [15] for staggered diamond pins provided the minimum MAE in this comparison.

5. Conclusions

Flow boiling experiments of HFE-7100 in staggered diamond micro-pin fins having a pin height of 1 mm and pin width of 0.6 mm were carried out. The working fluid was tested at 1, 1.5 and 2 bar inlet

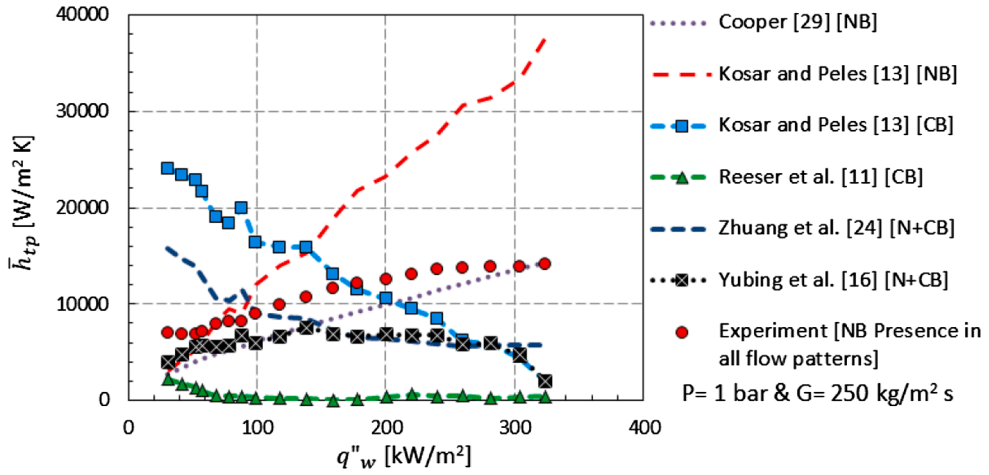

Fig. 23. Average two-phase heat transfer coefficient versus wall heat flux. NB: nucleate boiling, CB: convective boiling.

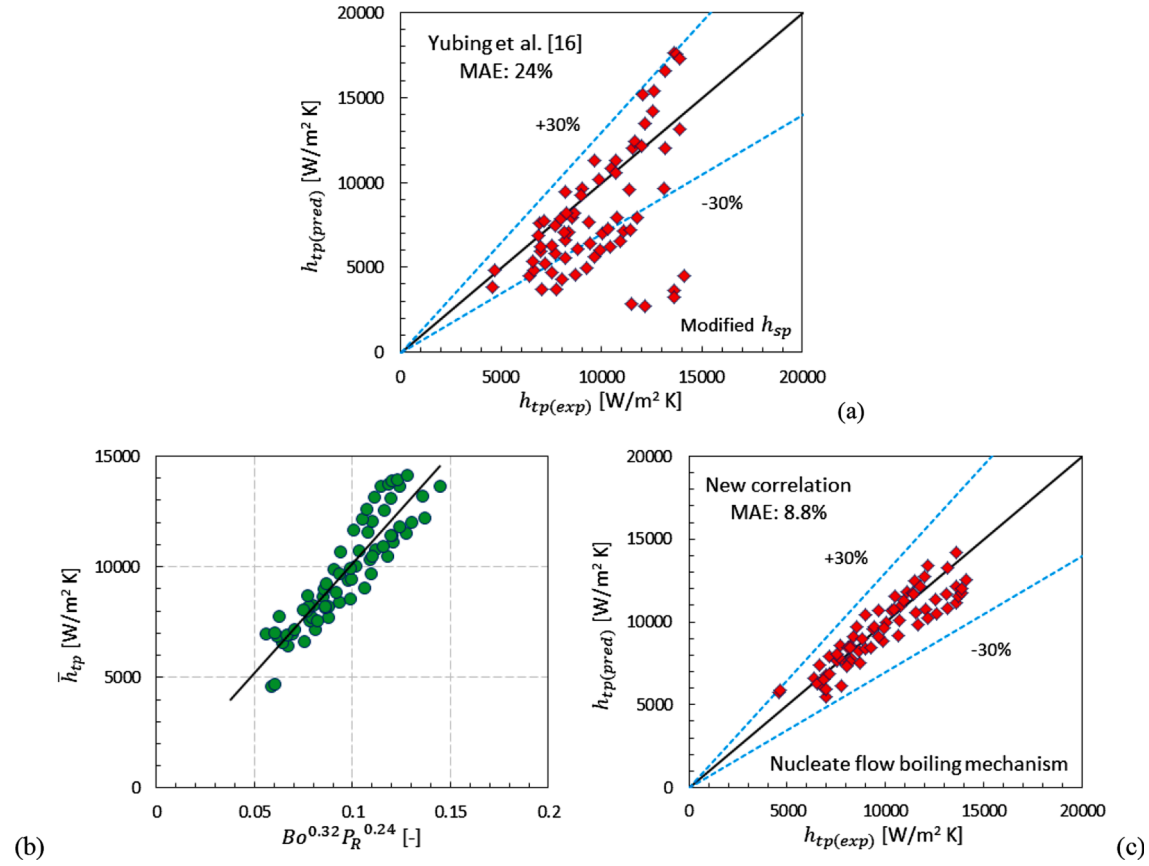

Fig. 24. Two-phase heat transfer coefficient: (a) modified correlation of [16], (b) two-phase heat transfer coefficient as a function of Bo and reduced pressure, (c) comparisons of present results with the new proposed correlation.

pressure, 5 K inlet degree of sub-cooling, mass flux of 100–250 kg/m^2 s and base heat flux up to 0.63 MW/m^2. The complex features of flow patterns were carefully captured and analysed using a high-resolution, high-speed camera. Heat transfer rates and pressure drop measurements were made. The results were reproducible and no hysteresis was observed. The main findings are summarised below.

Three different flow patterns were identified during the present study, namely: bubbly flow, mixed flow and vapour layer flow. Nucleation was clearly captured during all these flow regimes. However, the features of nucleating bubbles differed at the upstream and downstream sides of the pins due to different local pressure and inertia force. Pins could promote a stable liquid film around them with bubble nucleation occurring in the liquid film. Forward and zig-zag flow was captured, while flow reversal was not seen. Smaller bubbles, more nucleation sites and thicker liquid film were found when the inlet pressure increased from 1 to 2 bar.

The local and average two-phase heat transfer coefficient increased with increasing wall heat flux and inlet pressure. In contrast, the effect of mass flux was not significant within the studied range (100–250 kg/m^2 s), although it is worth noting that increasing the mass flux to 250 kg/m^2

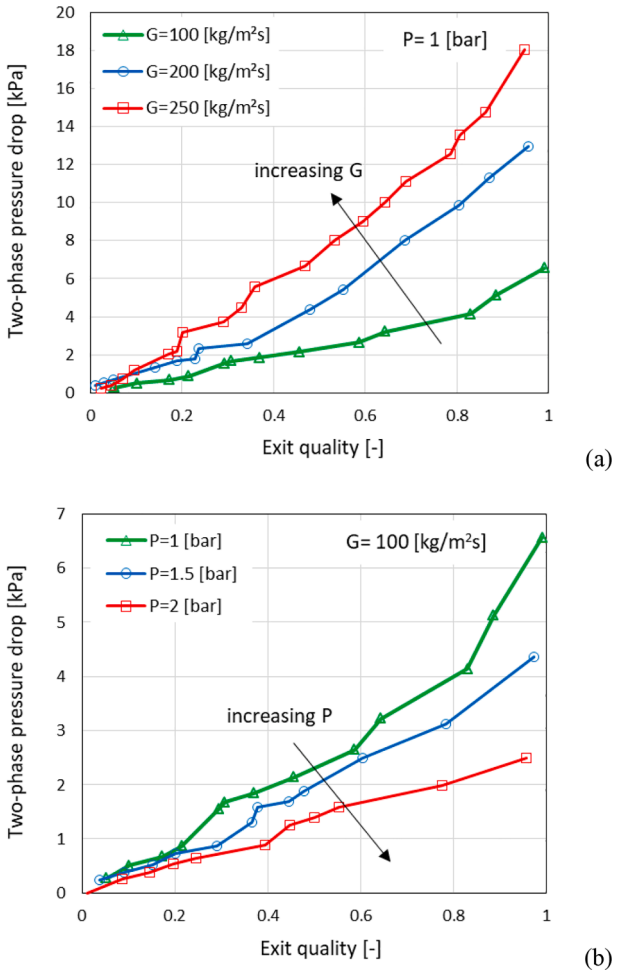

Fig. 25. Two-phase pressure drop at different operating conditions: (a) heat and mass flux effect (b) system pressure effect.

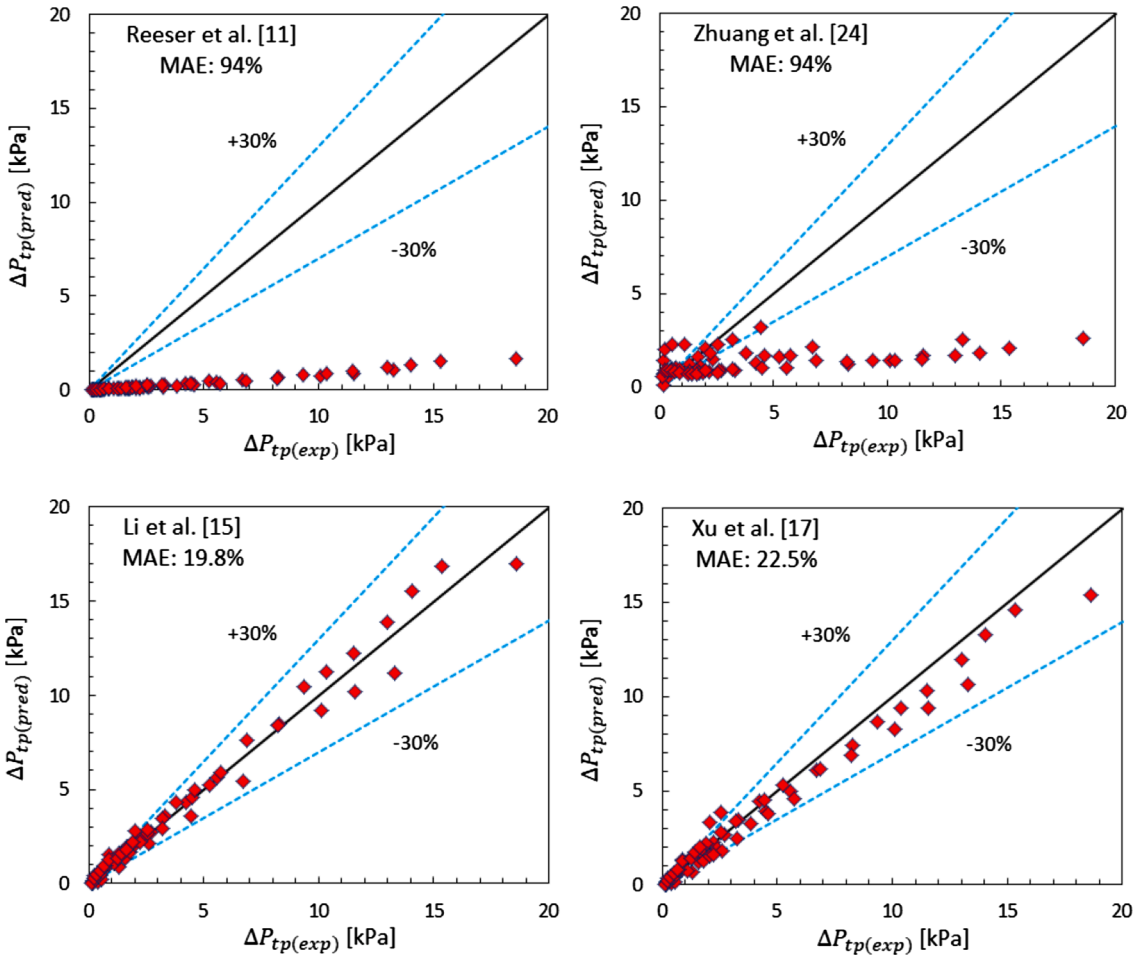

Fig. 26. Two-phase pressure drop comparison with correlations.

s resulted in an increase in the possible heat transfer rates without the occurrence of dryout regions or critical heat flux. The highest base heat flux of 0.63 MW/m^2 was reached with this design without occurrence of any thermal crisis, i.e. dryout region and critical heat flux. The highest wall heat flux was found to be 0.324 MW/m^2. The present geometric design demonstrated a stable thermal performance with acceptable working surface temperature for most electronics, i.e. less than 85 °C.

The two-phase pressure drop was found to increase with increasing wall heat flux and mass flux, while it decreased with increasing system pressure. It should be mentioned that the pressure drop across the heat sink examined was less than 18 kPa, indicating, firstly that the contribution of the pressure drop in the heat sink to the pumping power required in the complete thermal management system is not the critical design factor and secondly allowing the designer to focus on achieving the required heat dissipation rates. In a complete thermal management system, the entire system pressure drop in the system will be calculated

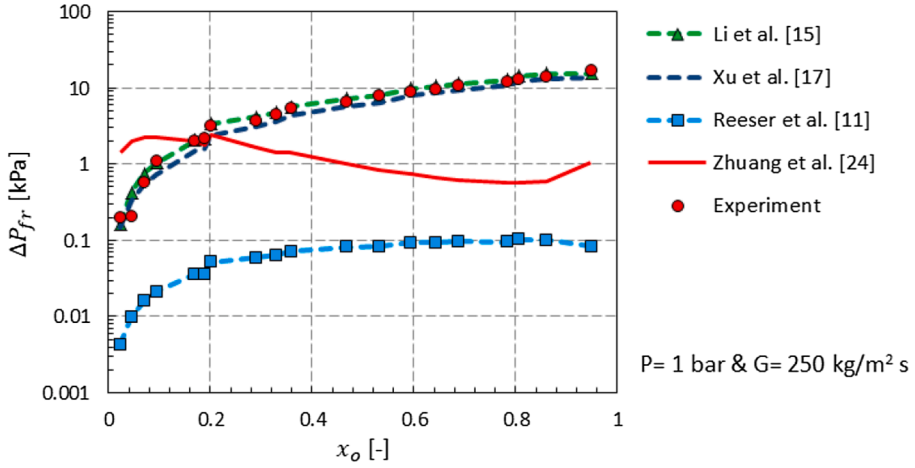

Fig. 27. Two-phase frictional pressure drop component versus exit vapour quality.

in order to size the pump required.

The evaluation of existing correlations showed that a good agreement between some of these heat transfer correlations and present results was found. In particular, the modified Yubing et al. [16] correlation showed good agreement with our results. The Boiling number and reduced pressure are the dominant parameters, with in the presence of nucleate boiling in the three flow regimes observed in the present study. A correlation of our results based on the Boiling number and reduced pressure, given in Eq. (41), can represent our data well for the specific range of parameters and the geometry of our study. Pressure drop correlations, which include the effect of pin dimensions and spacing in the two-phase friction multiplier provided better prediction of the current results. The correlations of Li et al. [15] and Xu et al. [17] showed good agreement with our results.

Further studies should be conducted in future work to assess these proposed correlations under different operating conditions. The effect of different design parameters such as pin shape, arrangement, dimensions and other working fluids should also be investigated. Additive manufacturing of micro-pin heat sinks is also recommended for future investigation. This could enable surface modifications and promote enhanced nucleation. Tip clearance, i.e. a gap between the cover plate and the pin tip, is another parameter that could affect the thermal performance, and should be considered. This could enhance fluid mixing above and behind the pins, while also increasing the total heat transfer area and overall heat transfer rates.

CRediT authorship contribution statement

Ali H. Al-Zaidi: Writing – review & editing, Writing – original draft, Visualization, Validation, Methodology, Investigation, Formal analysis. **Tassos G. Karayiannis:** Writing – review & editing, Writing – original draft, Validation, Supervision, Resources, Project administration, Methodology, Investigation, Funding acquisition, Formal analysis, Data curation, Conceptualization.

Declaration of competing interest

The authors declare that they have no known competing financial interests or personal relationships that could have appeared to influence the work reported in this paper.

Acknowledgement

The work was conducted with the support of the Engineering and Physical Sciences Research Council of the UK, under Grant: EP/T033045/1.

Appendix I

Two-phase heat transfer and pressure drop correlations, see Table 1 for more details.

Heat transfer coefficient

Kosar and Peles [13]:

For nucleate boiling mechanism:

$$h_{tp} = \frac{3.42 \times 10^7 q_w^{\circ\,1.01}}{\left(G_{max} i_{lg}\right)^{1.16}} + 0.12 h_{sp}^{0.7}$$

$$h_{sp} = \left(0.24 Re_l^{0.75} - 8.88\right) \frac{k_l}{D_h}$$

For convective boiling mechanism:

$$h_{tp} = 819 Re_l^{0.6} (1-x)^{0.22} \left(\frac{1-x}{x}\right)^{0.01}$$

Reeser et al. [11]:

$$h_{tp} = \xi \left(\varnothing_l^2\right)^{0.2475} h_{sp}$$

$$\varnothing_l^2 = 1 + \frac{0.24}{X} + \frac{1}{X^2}$$

$$\xi = C_1 e^{C_2 x} + C_3 x^3 + \left(\frac{C_4}{G_{max} + C_5}\right)^{0.5}$$

$$X = \left(\frac{\mu_l}{\mu_g}\right)^{0.274} \left(\frac{1-x}{x}\right)^{0.727} \left(\frac{\rho_g}{\rho_l}\right)^{0.5}$$

For HFE-7200 in in-line square pins:

$$C_1 = 2.47, C_2 = -9.2, C_3 = -1.71, C_4 = 45, C_5 = 181$$

$$Nu = 0.054 \left(\frac{S_L}{D_h}\right)^{0.2} \left(\frac{S_T}{D_h}\right)^{0.2} \left(\frac{H_{pin}}{D_h}\right)^{0.25} \left(1 + \frac{dh}{D_h}\right)^{0.4} Re^{0.6} Pr_l^{0.36} \left(\frac{Pr_l}{Pr_w}\right)^{0.25}$$

For HFE-7200 in staggered diamond pins:

$C_1 = 6, C_2 = -14.15, C_3 = -3.63, C_4 = 45, C_5 = 88$

$$Nu = 0.065\left(\frac{S_L}{D_h}\right)^{0.2}\left(\frac{S_T}{D_h}\right)^{0.2}\left(\frac{H_{pin}}{D_h}\right)^{0.25}\left(1+\frac{dh}{D_h}\right)^{0.4} Re^{0.6} Pr_l^{0.36}\left(\frac{Pr_l}{Pr_w}\right)^{0.25}$$

Yubing et al. [16]:

$$h_{tp} = \left[\left(Sh_{nb}\right)^2 + \left(Fh_{sp}\right)^2\right]$$

Cooper's correlation is used in h_{nb}.

$$h_{sp} = xh_{sp,g} + (1-x)h_{sp,l}$$

$$h_{sp,k} = \frac{Nu_k k_k}{D}$$

$$Nu_k = a\left(\frac{G_{max}D}{\mu_k}\right)^{0.95} {Pr_k}^{1/3}$$

$$a = 0.09\beta^{0.85}$$

$$S = 0.8We_l^{0.42}$$

$$We_l = \frac{(G_{max}(1-x))^2 D}{\rho_l \sigma}$$

$$F = 1 + 3.37exp\left[-\left(\frac{\left(\varnothing_l^2\right)^{0.2} - 1.72\beta^{-0.32}}{1.5}\right)^2\right]$$

$$\varnothing_l^2 = 1 + \frac{C}{X} + \frac{1}{X^2}$$

$$C = 1.82\beta^{-0.48}\omega^{-0.11}$$

$$X = \sqrt{\frac{f_l \frac{G_{max}^2(1-x)^2}{2\rho_l}}{f_g \frac{G_{max}^2 x^2}{2\rho_g}}}$$

$$f_k = a\frac{S_L}{D}\sqrt{1 + \frac{S_T^2}{4S_L^2}} Re_k^b + \varepsilon$$

$$a = 390.78\beta^{1.84}\omega^{-0.3}$$

$$b = -0.81 + 0.25\omega^{4.63}$$

$$\varepsilon = 24.93\beta^{1.68}\omega^{-0.2}$$

The following expressions are used in this correlation:

$$D = \frac{4H_{pin}(S_T - W_{pin})}{2(S_T - W_{pin} + H_{pin})}$$

$$\beta = \frac{W_{pin}L_{pin}}{2S_T S_L}$$

$$\omega = \frac{W_{pin}}{L_{pin}}$$

Subscript k: see Note below for more details.

Zhuang et al. [24]:

$$h_{tp} = \xi\left(\varnothing_l^2\right)^{0.275} h_{sp}$$

$$\xi = 9.698e^{-1.327x} + 1.746x^3$$

$$h_{sp} = \frac{Nuk_l}{D_h}$$

$$Nu = 8.444\left(\frac{S_L}{D_h}\right)^{0.2}\left(\frac{S_T}{D_h}\right)^{0.2}\left(\frac{H_{pin}}{D_h}\right)^{0.25}\left(1+\frac{W_b}{D_h}\right)^{0.4} Re^{0.6} Pr_l^{-2.361}\left(\frac{Pr_l}{Pr_w}\right)^{0.25}$$

$$\varnothing_l^2 = 1 + \frac{12.729}{X^{-0.176}} + \frac{1}{X^2}$$

$$X = \sqrt{\frac{f_l \frac{G_{max}^2(1-x)^2}{2\rho_l}}{f_g \frac{G_{max}^2 x^2}{2\rho_g}}}$$

$$f_k = 0.393 - \frac{20.709}{Re_k} + \frac{3.461\times10^3}{Re_k^2} + \frac{8.254\times10^4}{Re_k^3} - \frac{8.767\times10^4}{Re_k^4}$$

Cooper [29], pool boiling on copper surfaces:

$$h_{tp} = 95{*}P_R^{(0.12-0.2log_{10}R_{p,old})}\left[-log_{10}(P_R)\right]^{-0.55} M^{-0.5} q_w^{"0.67}$$

$R_{p,old} = \frac{Ra}{0.4}$(suggested by Gorenflo et al. [46])

Pressure drop

Reeser et al. [11]:

$$\left(\frac{dP}{dz}\right)_{fr} = \lambda\left(\frac{dP}{dz}\right)_l \varnothing_l^2$$

$$\varnothing_l^2 = 1 + \frac{C}{X} + \frac{1}{X^2}$$

$$X = \left(\frac{\mu_l}{\mu_g}\right)^{0.274}\left(\frac{1-x}{x}\right)^{0.727}\left(\frac{\rho_g}{\rho_l}\right)^{0.5}$$

$$f_l = C_f\left(\frac{S_L}{D_h}\right)^{0.2}\left(\frac{S_T}{D_h}\right)^{0.2}\left(\frac{H_{pin}}{D_h}\right)^{0.18}\left(1+\frac{dh}{D_h}\right)^{0.2} Re_l^{-0.435}$$

For HFE-7200 in in-line square pins:

$\lambda = 0.027, C = 5, C_f = 4.77$

For HFE-7200 in staggered diamond pins:

$\lambda = 0.044, C = 5, C_f = 2.89$

Li et al. [15]:

$$\varnothing_l^2 = 1 + \frac{C}{X} + \frac{1}{X^2}$$

$$C = 1.82\beta^{-0.48}\omega^{-0.11}$$

$$X = \sqrt{\frac{f_l \frac{G_{max}^2(1-x)^2}{2\rho_l}}{f_g \frac{G_{max}^2 x^2}{2\rho_g}}}$$

$$f_k = a\frac{S_L}{D}\sqrt{1+\frac{S_T^2}{4S_L^2}Re_k^b} + \varepsilon$$

$$a = 390.78\beta^{1.84}\omega^{-0.3}$$

$$b = -0.81 + 0.25\omega^{4.63}$$

$$\varepsilon = 24.93\beta^{1.68}\omega^{-0.2}$$

The following expressions are used in this correlation:

$$\beta = \frac{W_{pin} L_{pin}}{2 S_T S_L}$$

$$\omega = \frac{W_{pin}}{L_{pin}}$$

Zhuang et al. [24]:

$$\varnothing_l^2 = 1 + \frac{C}{X^{-0.176}} + \frac{1}{X^2}$$

$$C = 12.729$$

$$X = \sqrt{\frac{f_l \frac{G_{max}^2 (1-x)^2}{2\rho_l}}{f_g \frac{G_{max}^2 x^2}{2\rho_g}}}$$

$$f_k = 0.393 - \frac{20.709}{Re_k} + \frac{3.461 \times 10^3}{Re_k^2} + \frac{8.254 \times 10^4}{Re_k^3} - \frac{8.767 \times 10^4}{Re_k^4}$$

Xu et al. [17]:

$$\varnothing_l^2 = \left(1 + \frac{C}{X^{1.306}} + \frac{1}{X^{2.053}}\right) \frac{1}{La^{0.8}}$$

$$C = 1.653$$

$$X = \left(\frac{f_l}{f_g}\right)^{0.5} \left(\frac{1-x}{x}\right) \left(\frac{\rho_g}{\rho_l}\right)^{0.5}$$

$$f_k = \frac{29.28}{Re_{k,min}^{0.41}}$$

$$Re_{l,min} = \frac{G_{min}(1-x) D_{min}}{\mu_l}$$

$$Re_{g,min} = \frac{G_{min} x D_{min}}{\mu_g}$$

$$La = \sqrt{\frac{\sigma}{g(\rho_l - \rho_g) D_{min}^2}}$$

The following expressions are used in this correlation:

$$G_{min} = \frac{\dot{m}}{W_{min} H_{pin}}$$

$$D_{min} = \frac{4 W_{min} H_{pin}}{2(W_{min} + H_{pin})}$$

where W_{min} is the equivalent width related to the minimum transverse cross-sectional area. The void fraction by Xu and Fang [47] was used in their correlation:

$$\alpha = \left[1 + \left(1 + 2Fr_l^{-0.2} \alpha_h^{3.5}\right) \left(\frac{1-x}{x}\right) \left(\frac{\rho_g}{\rho_l}\right)\right]^{-1}$$

$$Fr_l = \frac{G_{max}^2}{g D_h \rho_l^2}$$

Homogeneous void fraction correlation:

$$\alpha_h = \left[1 + \frac{1-x}{x} \left(\frac{\rho_g}{\rho_l}\right)\right]^{-1}$$

Note

k refers to l for liquid or g for vapour. The following expressions are used in the abovementioned correlations:
Liquid Reynolds number:

$$Re_l = \frac{G_{max}(1-x)D_h}{\mu_l}$$

Vapour Reynolds number:

$$Re_g = \frac{G_{max}xD_h}{\mu_g}$$

Maximum mass flux:

$$G_{max} = \frac{\dot{m}}{A_{min}}$$

For staggered pins with $S_D > \frac{S_T+D_h}{2}$:

$$A_{min} = W_b H_{pin}\left[1 - \frac{D_h}{S_T}\right]$$

Hydraulic diameter D_h is found based on the pin cross-sectional area:

$$D_h = \frac{4W_{pin}L_{pin}}{2(W_{pin}+L_{pin})}$$

Data availability

Data will be made available on request.

References

[1] A.H. Al-Zaidi, M.M. Mahmoud, T.G. Karayiannis, Flow boiling in copper and aluminium microchannels, Int. J. Heat Mass Transf. 194 (2022) 123101.
[2] V.Y.S. Lee, T.G. Karayiannis, Influence of system pressure on flow boiling in microchannels, Int. J. Heat Mass Transf. 215 (2023) 124470.
[3] C.T. Lu, C. Pan, Stabilization of flow boiling in microchannel heat sinks with a diverging cross-section design, J. Micromech. Microeng. 18 (7) (2008) 075035.
[4] A.H. Al-Zaidi, M.M. Mahmoud, A. Ivanov, T.G. Karayiannis, Bubble nucleation site density, generation frequency and departure diameter in flow boiling of HFE-7100, Int. J. Heat Mass Transf. 242 (2025) 126830.
[5] W. Wan, D. Deng, Q. Huang, T. Zeng, Y. Huang, Experimental study and optimization of pin fin shapes in flow boiling of micro pin fin heat sinks, Appl. Therm. Eng. 114 (2017) 436–449.
[6] D. Deng, L. Zeng, W. Sun, G. Pi, Y. Yang, Experimental study of flow boiling performance of open-ring pin fin microchannels, Int. J. Heat Mass Transf. 167 (2021) 120829.
[7] W.T. Hsu, D. Lee, N. Lee, M. Yun, H.H. Cho, Enhancement of flow boiling heat transfer using heterogeneous wettability patterned surfaces with varying inter-spacing, Int. J. Heat Mass Transf. 164 (2021).
[8] B. Markal, B. Kul, O. Aydin, Comparative investigation of different types of expanding micro-pin-fin heat sinks at low mass flux, Int. Commun. Heat Mass Transf. 148 (2023) 107062.
[9] A.P. Moreira, A.G.da.S. Vilaronga, J.D. de Oliveira, E.M. Cardoso, Heat transfer and two-phase flow of deionized water in heat sink with micro-pin fins, Results Eng. 27 (2025) 106378.
[10] W. Li, J. Ma, C. Li, Enhanced flow boiling in microchannels by incorporating multiple micro-nozzles and micro-pinfin fences, Int. J. Heat Mass Transf. 165 (2021) 120695.
[11] A. Reeser, A. Bar-Cohen, G. Hetsroni, High quality flow boiling heat transfer and pressure drop in microgap pin fin arrays, Int. J. Heat Mass Transf. 78 (2014) 974–985.
[12] D.A. McNeil, A.H. Raeisi, P.A. Kew, P.R. Bobbili, A comparison of flow boiling heat-transfer in in-line mini pin fin and plane channel flows, Appl. Therm. Eng. 30 (16) (2010) 2412–2425.
[13] A. Kosar, Y. Peles, Boiling heat transfer in a hydrofoil-based micro pin fin heat sink, Int. J. Heat Mass Transf. 50 (2007) 1018–1034.
[14] J. Wang, S. Qi, Z. Xu, Y. Xu, Study on the flow boiling characteristics of novel pin fin heat sinks in a two-phase mechanically pumped cooling loop, Case Stud. Therm. Eng. 60 (2024) 104724.
[15] J. Li, D. Zhang, W. Yubing, W. Chen, G. Zhu, Pressure drop of R134a in mini channels with micro pin fins during flow boiling, Appl. Therm. Eng. 217 (2022) 119195.
[16] W. Yubing, J. Li, D. Zhang, W. Chen, G. Zhu, Investigation of the flow boiling performance in mini channel with micro pin fin, Heat Mass Transf. Und Stoffuebertragung 59 (8) (2023) 1543–1563.
[17] Y. Xu, L. Li, Z. Yan, Experimental investigations of the flow boiling characteristics of green refrigerants in a novel petaloid micropin-fin heat sink, Int. J. Heat Mass Transf. 212 (2023).
[18] C. Falsetti, H. Jafarpoorchekab, M. Magnini, N. Borhani, J.R. Thome, Two-phase operational maps, pressure drop, and heat transfer for flow boiling of R236fa in a micro-pin fin evaporator, Int. J. Heat Mass Transf. 107 (2017) 805–819.
[19] B. Hu, D. Qi, M. Lin, Q. Wang, A comparative study of flow boiling heat transfer and pressure drop characteristics in a pin-finned heat sink at horizontal / vertical upward flow orientations, ASME J. Heat Mass Transf. 146 (2024) 1–14.
[20] M. Law, P.S. Lee, A comparative study of experimental flow boiling heat transfer and pressure characteristics in straight- and oblique-finned microchannels, Int. J. Heat Mass Transf. 85 (2015) 797–810.
[21] L. Liu, L. Yu, B. Yuan, B. Liu, J. Wei, Flow boiling heat transfer enhancement via micro-pin-fins/ZnO nanorods hierarchical surface, Int. J. Heat Mass Transf. 203 (2023) 123810.
[22] X. Yu, C. Woodcock, Y. Wang, J. Plawsky, Y. Peles, Enhanced subcooled flow boiling heat transfer in microchannel with piranha pin fin, ASME J. Heat Transf. 139 (11) (2017) 1–13.
[23] J.M. Nunes, J.D. de Oliveira, J.B. Copetti, S.S. Gajghate, U. Banerjee, S.K. Mitra, E. M. Cardoso, J.M. Nunes, J.D. de Oliveira, J.B. Copetti, S.S. Gajghate, U. Banerjee, S.K. Mitra, E.M. Cardoso, Thermal performance analysis of micro pin fin heat sinks under different flow conditions, Energies 16 (2023) 3175.
[24] X. Zhuang, Y. Xie, X. Li, S. Yue, H. Wang, H. Wang, Experimental investigation on flow boiling of HFE-7100 in a microchannel with pin fin array, Appl. Therm. Eng. 225 (2023) 120180.
[25] X. Ji, X. Yang, X. Ma, H. Tian, J. Wei, B. Sunden, Two-phase flow characteristics and visualization of distributed confined array jet boiling, Case Stud. Therm. Eng. 57 (2024) 104345.
[26] X. Wang, M. Chen, D. Tate, H. Rahimi, S. Zhang, Numerical investigation on hydraulic and thermal characteristics of micro latticed pin fin in the heat sink, Int. J. Heat Mass Transf. 149 (2020) 119157.
[27] P. Bhandari, K.S. Rawat, Y.K. Prajapati, D. Padalia, L. Ranakoti, T. Singh, Design modifications in micro pin fin configuration of microchannel heat sink for single phase liquid flow: a review, J. Energy Storage 66 (2023) 107548.
[28] F. Mertens, S. Castagne, M.R. Vetrano, A review on flow boiling enhancement on textured surfaces, Energies 17 (2024) 558.
[29] M.G. Cooper, Heat flow rates in saturated nucleate pool boiling-a wide-ranging examination using reduced properties, Adv. Heat Transf. 16 (1984) 157–239.

[30] J.R. Thome, A. Cioncolini, Encyclopedia of two-phase heat transfer and flow, set 1: fundamentals and methods, Volume 3: Flow Boiling in Macro and Microchannels, Chapter 6: Two-Phase Pressure Drop. World Scientific Publishing, 2015.
[31] D. Chisholm, A theoretical basis for the Lockhart–Martinelli correlation for two-phase flow, Int. J. Heat Mass Transf. 10 (1967) 1767–1778.
[32] S.M. Zivi, Estimation of steady-state steamvoid-fraction by means of the principle of minimum entropy production, J. Heat Transf. 86 (1964) 247–252.
[33] A.H. Al-Zaidi, M.M. Mahmoud, T.G. Karayiannis, Flow boiling of HFE-7100 in microchannels: experimental study and comparison with correlations, Int. J. Heat Mass Transf. 140 (2019) 100–128.
[34] W. Li, J. Ma, T. Alam, F. Yang, J. Khan, C. Li, Flow boiling of HFE-7100 in silicon microchannels integrated with multiple micro-nozzles and reentry micro-cavities, Int. J. Heat Mass Transf. 123 (2018) 354–366.
[35] W. Qu, A. Siu-Ho, Measurement and prediction of pressure drop in a two-phase micro-pin-fin heat sink, Int. J. Heat Mass Transf. 52 (2009) 5173–5184.
[36] W. Qu, I. Mudawar, Measurement and prediction of pressure drop in two-phase micro-channel heat sinks, Int. J. Heat Mass Transf. 46 (15) (2003) 2737–2753.
[37] H.W. Coleman, W.G. Steele, Experimentation and uncertainty analysis for engineers, 3nd ed., Wiley, Chichester, New York, 2009.
[38] R.S. Prasher, J. Dirner, J.Y. Chang, A. Myers, D. Chau, D. He, S. Prstic, Nusselt number and friction factor of staggered arrays of low aspect ratio micropin-fins under cross flow for water as fluid, J. Heat Transfer 129 (2) (2007) 141–153.
[39] C.A. Konishi, R. Hwu, W. Qu, F.E. Pfefferkorn, Experimental study and numerical analysis of water single-phase pressure drop across a micro-pin-fin array, in: Proceedings of the 14th International Heat Transfer Conference IHTC14, 2010, pp. 1–9. Washington, DC, USA.
[40] F. Xu, H. Wu, Experimental study of water flow and heat transfer in silicon micro-pin-fin heat sinks, J. Heat Transfer 140 (12) (2018) 122401.
[41] A. Koşar, Y. Peles, Convective flow of refrigerant (R-123) across a bank of micro pin fins, Int. J. Heat Mass Transf. 49 (17–18) (2006) 3142–3155.
[42] M. Law, P.S. Lee, K. Balasubramanian, Experimental investigation of flow boiling heat transfer in novel oblique-finned microchannels, Int. J. Heat Mass Transf. 76 (2014) 419–431.
[43] B. Markal, B. Kul, M. Avci, R. Varol, Effect of gradually expanding flow passages on flow boiling of micro pin fin heat sinks, Int. J. Heat Mass Transf. 197 (2022) 123355.
[44] M.M. Mahmoud, T.G. Karayiannis, Pool boiling review: part I - fundamentals of boiling and relation to surface design, Therm. Sci. Eng. Prog. 25 (2021) 101024.
[45] E.M. Fayyadh, M.M. Mahmoud, K. Sefiane, T.G. Karayiannis, Flow boiling heat transfer of R134a in multi microchannels, Int. J. Heat Mass Transf. 110 (2017) 422–436.
[46] D. Gorenflo, U. Chandra, S. Kotthoff, A. Luke, Influence of thermophysical properties on pool boiling heat transfer of refrigerants, Int. J. Refrig 27 (2004) 492–502.
[47] Y. Xu, X. Fang, Correlations of void fraction for two-phase refrigerant flow in pipes, Appl. Therm. Eng., 64 (2014) 242e251 Contents.